LAWRENCE
LIVERMORE
NATIONAL
LABORATORY

Ultraviolet Resonant Raman Enhancements in the Detection of Explosives

B. J. Short, J. C. Carter

June 9, 2009

Disclaimer

NAVAL POSTGRADUATE SCHOOL

MONTEREY, CALIFORNIA

THESIS

ULTRAVIOLET RESONANCE RAMAN ENHANCEMENTS IN THE DETECTION OF EXPLOSIVES

by

Billy Joe Short, Jr.

June 2009

Thesis Advisor:	Craig F. Smith
Second Reader:	J. Chance Carter

THIS PAGE INTENTIONALLY LEFT BLANK

REPORT DOCUMENTATION PAGE			*Form Approved OMB No. 0704-0188*
Public reporting burden for this collection of information is estimated to average 1 hour per response, including the time for reviewing instruction, searching existing data sources, gathering and maintaining the data needed, and completing and reviewing the collection of information. Send comments regarding this burden estimate or any other aspect of this collection of information, including suggestions for reducing this burden, to Washington headquarters Services, Directorate for Information Operations and Reports, 1215 Jefferson Davis Highway, Suite 1204, Arlington, VA 22202-4302, and to the Office of Management and Budget, Paperwork Reduction Project (0704-0188) Washington DC 20503.			
1. AGENCY USE ONLY *(Leave blank)*	**2. REPORT DATE** June 2009	**3. REPORT TYPE AND DATES COVERED** Master's Thesis	
4. TITLE AND SUBTITLE Ultraviolet Resonance Raman Enhancements in the Detection of Explosives		**5. FUNDING NUMBERS** Contract DE-AC52-07NA27344	
6. AUTHOR(S) Billy Joe Short, Jr.			

7. PERFORMING ORGANIZATION NAME(S) AND ADDRESS(ES)
    Naval Postgraduate School
    Monterey, CA 93943-5000
		8. PERFORMING ORGANIZATION REPORT NUMBER
		LLNL-TH-4113751	

9. SPONSORING /MONITORING AGENCY NAME(S) AND ADDRESS(ES)
    Lawrence Livermore National Laboratory
    Livermore, California
		10. SPONSORING/MONITORING AGENCY REPORT NUMBER	

11. SUPPLEMENTARY NOTES The views expressed in this thesis are those of the author and do not reflect the official policy or position of the Department of Defense or the U.S. Government.			
12a. DISTRIBUTION / AVAILABILITY STATEMENT Approved for public release; distribution is unlimited.		**12b. DISTRIBUTION CODE** A	

13. ABSTRACT (maximum 200 words)

Raman-based spectroscopy is potentially militarily useful for standoff detection of high explosives. Normal (non-resonance) and resonance Raman spectroscopies are both light scattering techniques that use a laser to measure the vibrational spectrum of a sample. In resonance Raman, the laser is tuned to match the wavelength of a strong electronic absorbance in the molecule of interest, whereas, in normal Raman the laser is not tuned to any strong electronic absorbance bands. The selection of appropriate excitation wavelengths in resonance Raman can result in a dramatic increase in the Raman scattering efficiency of select band(s) associated with the electronic transition. Other than the excitation wavelength, however, resonance Raman is performed experimentally the same as normal Raman. In these studies, normal and resonance Raman spectral signatures of select solid high explosive (HE) samples and explosive precursors were collected at 785 nm, 244 nm and 229 nm. Solutions of PETN, TNT, and explosive precursors (DNT & PNT) in acetonitrile solvent as an internal Raman standard were quantitatively evaluated using ultraviolet resonance Raman (UVRR) microscopy and normal Raman spectroscopy as a function of power and select excitation wavelengths. Use of an internal standard allowed resonance enhancements to be estimated at 229 nm and 244 nm. Investigations demonstrated that UVRR provided ~2000-fold enhancement at 244 nm and ~800-fold improvement at 229 nm while PETN showed a maximum of ~25-fold at 244 nm and ~190-fold enhancement at 229 nm solely from resonance effects when compared to normal Raman measurements. In addition to the observed resonance enhancements, additional Raman signal enhancements are obtained with ultraviolet excitation (i.e., Raman scattering scales as v^4 for measurements based on scattered photons). A model, based partly on the resonance Raman enhancement results for HE solutions, is presented for estimating Raman enhancements for solid HE samples.

14. SUBJECT TERMS Raman Spectroscopy, Standoff Detection, High Explosives, Explosive Detection, Inelastic Scattering, Resonance Raman			**15. NUMBER OF PAGES** 102
			16. PRICE CODE
17. SECURITY CLASSIFICATION OF REPORT Unclassified	**18. SECURITY CLASSIFICATION OF THIS PAGE** Unclassified	**19. SECURITY CLASSIFICATION OF ABSTRACT** Unclassified	**20. LIMITATION OF ABSTRACT** UU

THIS PAGE INTENTIONALLY LEFT BLANK

ULTRAVIOLET RESONANCE RAMAN ENHANEMENT IN THE DETECTION
OF EXPLOSIVES

Billy J. Short, Jr.
Major, United States. Marine Corps
B.S. in Chemistry, Towson State University, 1994
MAS. in Chemistry (Analytical Chemistry), Illinois Institute of Technology, 2007

Submitted in partial fulfillment of the
requirements for the degree of

MASTER OF SCIENCE IN APPLIED PHYSICS

from the

NAVAL POSTGRADUATE SCHOOL
June 2009

Author: Billy Joe Short, Jr.

Approved by: Craig Smith
                 Thesis Advisor

                 J. Chance Carter
                 Second Reader

                 James Luscombe
                 Chairman, Department of Physics

THIS PAGE INTENTIONALLY LEFT BLANK

ABSTRACT

Raman-based spectroscopy is potentially militarily useful for standoff detection of high explosives. Normal (non-resonance) and resonance Raman spectroscopies are both light scattering techniques that use a laser to measure the vibrational spectrum of a sample. In resonance Raman, the laser is tuned to match the wavelength of a strong electronic absorbance in the molecule of interest, whereas, in normal Raman the laser is not tuned to any strong electronic absorbance bands. The selection of appropriate excitation wavelengths in resonance Raman can result in a dramatic increase in the Raman scattering efficiency of select band(s) associated with the electronic transition. Other than the excitation wavelength, however, resonance Raman is performed experimentally the same as normal Raman. In these studies, normal and resonance Raman spectral signatures of select solid high explosive (HE) samples and explosive precursors were collected at 785 nm, 244 nm and 229 nm. Solutions of PETN, TNT, and explosive precursors (DNT & PNT) in acetonitrile solvent as an internal Raman standard were quantitatively evaluated using ultraviolet resonance Raman (UVRR) microscopy and normal Raman spectroscopy as a function of power and select excitation wavelengths. Use of an internal standard allowed resonance enhancements to be estimated at 229 nm and 244 nm. Investigations demonstrated that UVRR provided ~2000-fold enhancement at 244 nm and ~800-fold improvement at 229 nm while PETN showed a maximum of ~25-fold at 244 nm and ~190-fold enhancement at 229 nm solely from resonance effects when compared to normal Raman measurements. In addition to the observed resonance enhancements, additional Raman signal enhancements are obtained with ultraviolet excitation (i.e., Raman scattering scales as ν^4 for measurements based on scattered photons). A model, based partly on the resonance Raman enhancement results for HE solutions, is presented for estimating Raman enhancements for solid HE samples.

THIS PAGE INTENTIONALLY LEFT BLANK

TABLE OF CONTENTS

LIST OF FIGURES

x

LIST OF TABLES

THIS PAGE INTENTIONALLY LEFT BLANK

ACKNOWLEDGMENTS

Foremost I wish to thank my wife, Sandra, and my family for their unconditional love and support especially during my time at the USS 'Library' and to Livermore, CA.

I wish to thank Professor Smith for his extraordinary efforts in arranging this unique research opportunity for me. The research was enjoyable and rewarding and it wouldn't have been possible without his efforts. I also wish to thank Professor Larraza for juggling my schedule to free up the research time required to make this thesis possible. To Dr. Chance Carter I wish to express my deep gratitude for taking the time to help devise a research plan that was fully supportable given time and other experimental constraints. He took the time to teach me new skill sets, help foresee and avoid research pitfalls, and provided the laboratory resources and Raman expertise required for a successful project. His support and guidance helped me tremendously and I am very grateful for his efforts.

I am grateful to George Solhan and Lee Mastroianni of the Office of Naval Research (ONR) and to Larry Mixon & crew at Naval Surface Warfare Center Panama City for resourcing and providing the an improved ICCD detector. Additionally, Dr. John Wilkinson of Naval Surface Warfare Center-Indian Head helped identify the source of desensitizing impurities found in one of our explosive samples (PETN).

THIS PAGE INTENTIONALLY LEFT BLANK

I. INTRODUCTION

A. MOTIVATION

The development of reliable and effective explosive detection technologies is an important challenge for military and homeland security applications. From the wide proliferation of landmines, termed the poor man's artillery, to the pressing need to detect improvised explosive devices, the need for a dependable and effective explosive detection system is becoming increasingly important. Due to the extreme challenges that hinder effective explosive detection, it is widely recognized that there is no "silver bullet" solution. Several challenges hinder the development and deployment of standoff explosive detection systems. Landmines and improvised explosive devices (IED) are intentionally concealed explosives designed to thwart detection efforts. Additionally, most commercial and military grade explosives exhibit extremely low vapor pressures, which significantly limits the ability to detect explosives in the gas phase at standoff distances or otherwise. Every explosive detection system developed or theorized to date has drawbacks when evaluated against the following factors: minimum detectable limit of explosive concentrations, probability of detection, probability of false alarms, the variety of explosives that can be reliably detected, portability of the unit, required analysis time, standoff capability, container or soil penetration capabilities, required operator training, and the cost of the system.

Due to the numerous and ever changing number of ways that explosives are used against military personnel and equipment, it is important to develop a suite of explosives detection technologies. For example, technologies developed to detect landmines may be unsuitable to detect explosives on a suicide bomber. The chemistry and physics of explosive detection leads to cases where one technology is very effective within inches of the explosives (e.g., used in personnel screening) but would be completely ineffective at standoff distances. For these reasons a layered and multifaceted approach to landmines and IED defense is necessary.

1

Currently, there are a variety of techniques used to detect explosives: sniffing explosive vapors (e.g., fluorescence quenching and ion mobility spectroscopy), imaging bulk explosives (e.g., x-ray backscattering and millimeter wave imaging), and spectroscopic detection of explosives (e.g., infrared, Raman, and laser-induced breakdown spectroscopy techniques, and nuclear techniques). Due to the drawbacks experienced by all explosive detection systems, it is highly desirable to combine detection systems in orthogonal approaches [1], meaning detection methods should significantly differ in detection modality to capitalize upon the strengths of individual techniques while minimizing overall system weaknesses. When orthogonal systems are used optimally it is possible to obtain a probability of detection and false alarm rate that is more favorable than any individual detection modality.

This research focuses on fundamental aspects of resonance Raman spectroscopy as applied to select HE materials to advance our current understanding and potentially improve HE detection at standoff distances.

B. BACKGROUND OF PREVIOUS WORK

Previous research into standoff detection of explosives using Raman spectroscopy conducted by J. C. Carter's research group at Lawrence Livermore National Laboratory and S. K. Sharma's research group at the University of Hawaii provide the foundation of this investigation. Each of the aforementioned research groups has completed experiments that demonstrate the initial feasibility of using normal Raman spectroscopy to detect explosives at standoff distances; however, it is a much greater challenge to demonstrate a technology's military utility since this involves proposed concepts of operations, theorizing system required performance parameters, and utilizing more representative target sets.

The work completed in this thesis exploits the previous results derived from work from several research groups investigating standoff Raman and resonance Raman to further improve the ability to detect high explosives at standoff distances by assessing the potential gains achievable using resonance Raman to detect explosives.

2

C.   RESEARCH GOALS

The primary goal of this research is to demonstrate and quantify the improvements obtainable using resonance Raman spectroscopy to detect high explosives.

D.   RESEARCH OBJECTIVES

The primary research objectives were developed to achieve the stated research goal. The key objectives include the following: (1) performing absorption studies of select HE materials (e.g., TNT, PETN, PNT, DNT) to determine absorption bands throughout the UV-Vis spectral region for acquiring UV Raman spectral signatures; (2) performing solution-based, UV-excited, Raman HE measurements while utilizing an internal Raman standard measured in-situ; (3) determining the resonance Raman signal enhancements, if any, from the solution-based HE measurements relative to normal Raman (4) investigate experimental parameters in terms of two different UV wavelengths, and select laser power settings.

THIS PAGE INTENTIONALLY LEFT BLANK

II.   DETECTION OF EXPLOSIVES

A.   SELECT PROPERTIES OF EXPLOSIVES

Explosives are unstable molecules that can share many similar physical characteristics. Most military explosives tend to have a melting point greater than 80°C, have densities typically between 1.6 and 2.0, and they are thermally stable and relatively insensitive to shock and other stimuli [2]. High explosives have low densities since they are comprised of low atomic number (Z) atoms like carbon, nitrogen oxygen, and hydrogen. High explosives, with some notable exceptions such as peroxide-based explosives, contain one or more nitro functional groups ($-NO_2$) that tend to be the least stable bond in the explosive molecule [3]. While most explosive compounds contain nitro groups, the organic chemistry of explosives can vary widely. Explosive molecules can be classified into several organic chemistry groups including open and closed chain nitro-aliphatic, nitrate esters (e.g., NC, NG, PETN), and nitramines (e.g., RDX, HMX) and aromatic compounds (e.g., PNT, DNT, TNT).

1.   Types of Explosives and Chemical Composition

Due to stability and availability, commercial and military grade explosives are the types of explosives most frequently encountered on today's battlefield. The elemental composition of oxygen and nitrogen is unusually high in most military explosives compared to other innocuous compounds, an exploitable feature for some analytical detection techniques. The homemade explosive triacetone triperoxide (TATP) is at the top of the list of notable exceptions to this rule of thumb; while it contains a high percentage of oxygen it does not contain nitrogen atoms. The average nitrogen and oxygen contents of explosives are 31 ± 12% nitrogen and 45 ± 8% oxygen [4].
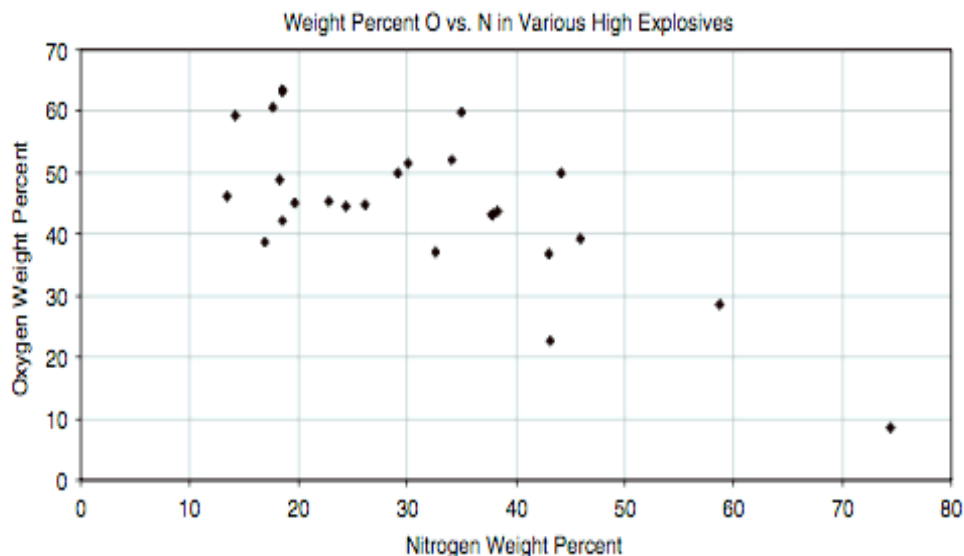
Figure 1.   Weight percent of oxygen and nitrogen in select high explosives (From: [4]).

2. Peroxide-based Explosives

In 2001, the US encountered homemade peroxide-based explosives when Richard Reid attempted to detonate PETN (pentaerythritol tetranitrate) with TATP on a Miami bound Boeing 767 flight. TATP was also used in the London public transit system bombings in 2005, and it has been a popular choice among homicide bombers for decades since it is very easy to synthesize. Before Operation IRAQI FREEDOM, TATP was one of the most common constituents used in IEDs, since it is effective and could be manufactured with easily obtained ingredients. The major drawback with TATP is its instability, which makes handling and synthesis dangerous. When factors allow groups to readily obtain commercial or military explosives, these will be preferred over peroxide-based explosives for performance and safety reasons. TATP has a significantly higher vapor pressure than most military explosives; for a given mass, TATP has approximately 10^4 more molecules in the air at room temperature than TNT (2,4,6-trinitrotoluene or also 2,4,6-TNT) [4].

6

B.   SPECTROSCOPY OF EXPLOSIVES

Spectroscopy was traditionally defined as the study of interaction of electromagnetic radiation with matter as a function of wavelength [5]. This includes the transmission, absorption, scattering and emission of light from the sample.   This definition was later expanded to encompass other forms of analytical measurements that include particles interacting with matter. After the analyte is perturbed, several different observable phenomena may be detected to provide characteristic information concerning the probed atom or molecule. Spectroscopic measurements may be based on absorption, scattering, or characteristic photon emissions. Several different forms of spectroscopy have been developed to probe solid, liquid and vapor phase explosives to provide qualitative and quantitative information. A recent publication by D. S. Moore [6] provides a thorough review on this topic.

1.   Explosive Vapors

Most high explosives have exceedingly low vapor pressures (see Figure 2), so very few molecules in the gas phase are present outside the solid or liquid explosive containing device. The concentration of most military grade high explosives present in the gas phase at room temperature can be measured in parts per tillion (ppt) to parts per million (ppm). As an example, converting this concentration to more familiar units yields approximately 0.1 ng/cm^3 for 2,4,6-TNT [7]. Some homemade peroxide-based explosives, like triacetone triperoxide (TATP), have considerably higher vapor pressures that can be measured in parts per thousand.
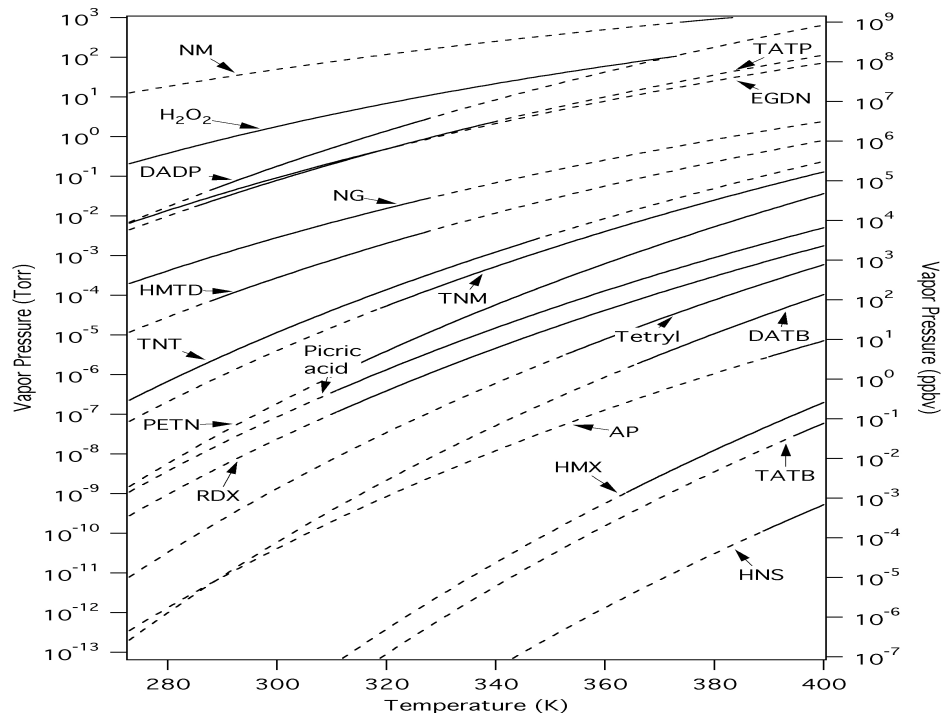
Figure 2.   Vapor Phase Concentration of common explosives as a function of temperature. The solid lines indicate experimental values (From: [6]).

In addition to the extremely low concentration of explosive molecules present in the gas phase under normal conditions, nitrogen based high explosives have a tendency to rapidly condense onto aerosols or solid surfaces rather than remain in the vapor phase further hindering detection efforts.

Canines have an exceptionally acute sense of smell and have typically been the gold standard for explosive vapor detection, however some trace detection systems have recently demonstrated improved sensitivities over canine detection by detecting sub-picogram quantities of select explosives [8]. Even with this exceptional sensitivity, it is difficult to detect explosive vapors using a point sensor at distances greater than a few meters. Sometimes favorable wind conditions can extend the range of explosive vapor detection, however, localizing such sources from turbulent plumes over extended distances with point sensors has not been demonstrated to date.

8

The presence of explosive related materials (ERM) such as tagging agents, impurities, reaction byproducts, plasticizers or decomposition products or enhancers such as propane in explosive devices may be more tractable than direct detection of the gas phase explosive molecules since ERM and enhancers tend to have much higher vapor pressures. The United Nation's International Civil Aviation Organization (ICAO) requires the addition of tagging agents to high explosives to aid in explosive detection [9]. Tagging agents are added in quantities varying from 0.1 to 0.5% by weight. 2-nitrotoluene and 4-nitrotoluene (PNT) are two of the four commonly used taggants to facilitate improved vapor detection of explosives. Natural impurities left over from the chemical reaction typically aid explosives detection efforts. For example, 2,4-dinitrotoluene (2,4-DNT) is found in TNT due to incomplete nitration reactions. DNT has a higher vapor pressure than TNT and is more easily detected than TNT itself [1, 9].

2. Bulk Explosives

A few spectroscopic methods have been developed to probe bulk explosives. Since explosives in landmines or IEDs are concealed by soil or in vehicles or under clothing, bulk spectroscopy methods must be capable of penetrating multiple inches of concealing material. Direct line-of-site detection techniques, such as Raman and LIBS, are very limited in such scenarios as signal transduction into and out of the device is often limited. Bulk detection methods typically have limited sensitivities that make it difficult or impossible to detect small antipersonnel mines that contain 50 to 100 g of high explosives, and the excitation source typically must be less than a few meters from the target. Even so, there are a few bulk detection methods such as pulsed fast and thermal neutron analysis (PFTNA) that are useful for bulk explosives detection. PFTNA uses energetic neutrons to probe high explosives though several layers of concealing materials to cause characteristic gamma ray emissions that can be detected by scintillators [10]. In this method, and similar to other bulk detection methods, the neutron source must be within inches or at most a few meters from the target to make a qualitative determination of the presence of explosives. Nuclear quadrupole resonance (NQR) is another bulk

detection method proven effective in handheld landmine detection at close distances by probing the magnetic dipole moments of ^{14}N in bulk explosives [11].

3.   Surface Residues

The surfaces of conventional and improvised munitions are contaminated with explosive residues [12, 13]. While concentrations of these explosive contaminants can vary, trace quantities can be readily detected by trace detection techniques (e.g., ion mobility spectroscopy and fluorescence quenching). Additionally, the transfer of explosive residues while handling explosives is typically unavoidable. Personnel involved in the storage, transportation and emplacement of mines and IEDs typically have identifiable amounts of explosive residues on their hands, clothes and personal effects, and this contamination can extend to vehicles, residences and other items that come into contact with the contaminated individual [14]. Explosives are very polar molecules and tend to strongly physisorb to many substrates. Most military grade explosives can be detected on persons who handle explosives over 48 hours past the time of exposure even when vigorous washing with surfactants is performed [13]. The typical quantity of explosives found in the fingerprints of contaminated individuals is approximately 40 to 100 μg of material [7, 14]. Raman microscopy (table-top device) measurements of explosive residues are used in forensic investigations [30].

One must consider the preexisting background levels of explosives and environmental degradation of explosive residues as important analytical considerations when detecting explosive residues.

4. Other Detectable Characteristics

While this thesis focuses on spectroscopic detection of explosives using Raman-based spectroscopy, there are other notable characteristics of explosives that can be exploited. These characteristics include: dielectric constants, & density. X-ray absorption and backscatter techniques have been successfully employed at close ranges by exploiting the characteristic densities of high explosive compounds.

While direct standoff detection of the explosive constituents is considered the 'Holy Grail' of landmine and IED detection, other non-direct detection modalities can be employed that rely on the device's metal content, radar signature, placement (e.g., disturbed soil), seismic signature, electronic signature, infrared heat signature, or ease of early detonation. It is commonly recognized that an effective explosive detection system will employ orthogonal detection modalities or methods that rely on independent measurements [1]. The use of orthogonal approaches can improve the probability of detecting explosives while reducing false alarm rates and protecting against simple countermeasures.

C.   REQUIRED SYSTEM PERFORMANCE

Fielding an effective and reliable tactical standoff explosive detection system is a daunting challenge. The basic concepts that must be addressed are presented below.

1.   Limit of Detection (LOD)

The limit of detection (LOD) for a given sensor is a critical figure of merit. In spectroscopy, the LOD is typically defined as an analyte signal that has a signal-to-noise ratio of two or three depending on the confidence interval of the measurement [1]. The ideal standoff tactical explosive detection systems is capable of detecting bulk explosives through the concealing materials, detecting extremely low concentrations of explosive vapors, or detecting trace explosive residues. Normal and resonance Raman spectroscopy lack the ability to detect explosive molecules in the vapor phase at standoff distances. Additionally, the direct-line-of-site requirement for Raman measurements is severely limiting for explosives detection scenarios requiring the penetration of concealing materials. The most likely scenario for standoff Raman-based detection involves direct-line-of-site measurements of HE or explosive related material residues.

2.   Time per Analysis

The time per analysis in Raman spectroscopy is the total required time to interrogate the sample via laser excitation, to detect the return analyte signal at a

specified confidence, and to process the data and report. For forensic or intelligence gathering purposes, a time per analysis of a few minutes may be suitable for combat situations; however, tactical situations require rapid detection and identification. Ideally a standoff detection method with very rapid time per analysis is employed to allow continuous sampling from a moving vehicle at some tactical rate of advance. In cases where the time per analysis is more protracted, the detection system may be more suitable as a confirmation tool that is employed after visual detection or other explosive detection means are employed.

3.   Specificity

The specificity of an analytical method is the ability of the instrument to correctly identify the desired analytes in a representative sample matrix [15]. Ideally, the system must be capable of detecting the analyte in the presence of interferences while not triggering a false positive alarm. Interferences vary and may include similar chemical moieties that produce signatures similar to that of the analyte. For example, an explosive detector ideally will not alarm on the presence of nitrogen containing fertilizers or other innocuous chemical compounds that may be routinely encountered, otherwise, the detector's effectiveness may be diminished. Convolution of spectral peaks can also occur due to matrix effects, which may hinder or preclude explosive detection efforts. As an example, standoff Raman-based measurements are capable of detecting O_2 and N_2 in air, which could obscure or completely mask the Raman band of a target analyte.

4.   Robustness

The robustness of an analytical technique is always an important consideration; however, in the military this metric is tested to extremes. It is a measure of the ability of the analytical method to retain its effectiveness despite intentional perturbations to the system [15]. For example, the ideal military explosive detectors should be equally capable of detecting explosives in -20^oF temperatures as well as temperatures reaching 130^oF. Additionally, the system should remain effective despite changes in relative humidity, precipitation, ambient light conditions, and changes to the sample matrix (i.e.,

the explosive may be located in different matrices and/or on different substrates etc.). In military explosive detection operations, the matrix and/or substrate for a given sample will most likely not be known á priori and background subtraction from these and other interferences may not be possible or feasible. Generally, speaking Raman measurements of real-world samples are always background noise limited.

Finally, detection systems must be designed with the warfighter in mind. Such systems must conform to the warfighters tactical situations in terms of robustness and ease of use including training requirements. Soldiers on the move should not be burdened with performing spectral matches even if technical reachback capabilities are available. The system should simply be capable of signaling an alarm to the presence of explosives at a given confidence level, localize the detection event, and if desired indicate the type of explosive that was detected with an indicated confidence level.

THIS PAGE INTENTIONALLY LEFT BLANK

III. FUNDAMENTALS OF RAMAN SPECTROSCOPY

A. SCATTERING PROCESSSES

Incident light on a surface will be scattered, absorbed, or pass directly through the material. Historically the study of light has inspired much of the theoretical and experimental work performed in physics. The nature of light scattering in the sky inspired Rayleigh's important contributions to the nature and behavior of light [16]. Both Lord Rayleigh and Sir Raman made fundamental discoveries in physics inquiring about the scattering of light.

1. Raleigh Scattering

There are several factors that determine the type of scattering that is observed when light interacts with matter, but the main factors include the refractive index of a particle on a substrate and the size of a particle compared to the wavelength of incident light [5]. Rayleigh scattering is an elastic scattering process that occurs when the diameter of the particles ($d_{particle}$) in the sample have much smaller dimensions than the wavelength (λ) of the incident electromagnetic waves ($d_{particle} < 0.05\lambda$) [5].

For a given Raman measurement, Rayleigh scattering is orders of magnitude more intense than the Raman scattered light. For this reason, Rayleigh scattering must be filtered before reaching the Raman detector.

2. Raman Scattering

The deep blue colors of the Mediterranean Sea observed by Sir Raman in the early 1920s inspired spectroscopy discoveries in a newly discovered scattering phenomenon now known as the Raman effect [16]. While Rayleigh scattering, centered at the incident wavelength, is the dominant scattering effect for the interaction of light with matter, a weaker, shifted Raman effect is also observed. The Raman effect is significantly weaker than Rayleigh scattering and only involves one Raman scattering for

approximately every 10^8 to 10^{10} incident photons [17, 18]. The oscillating electric field of the incident laser excitation interacts with matter; a short-lived distortion of a molecule's electron cloud perturbed by vibrations of the molecule gives rise to the Raman effect. The Raman effect will bathochromic (red) shift and hypsochromic (blue) shift light by two separate processes known as Stokes and anti-Stokes scattering, with Stokes scattering being the dominant effect. In Stokes scattering a molecule in the ground vibrational state is excited to a virtual state (i.e., not a real state in the molecule), which nearly simultaneously emits a less energetic red shifted photon. In anti-Stokes scattering, a molecule in an excited vibrational state imparts energy to the incident photon and relaxes back to the ground vibrational state by emitting a blue-shifted photon. The energy level diagram shown in Figure 3 depicts the Rayleigh, Stokes and anti-Stokes scattering processes with the *m* state representing the ground state and the *n* state representing an arbitrary excited state.
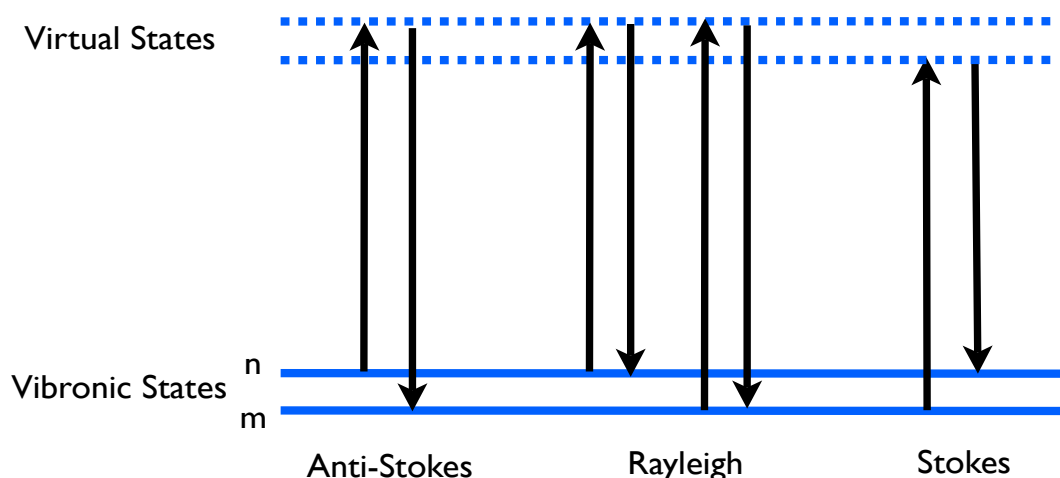
Figure 3.   Energy level diagram of normal inelastic Raman processes and Rayleigh scattering (After: [18]). At ambient temperature explosive molecules are mostly in the ground state (m) and the Stokes effect dominates the Raman scattering processes. Rayleigh scattering is an elastic scattering effect. In resonance Raman techniques, which will be discussed later, the molecule is excited to an electronic transition.

At ambient temperatures, most molecules are in the ground state and therefore, Stokes scattering intensity is much stronger than anti-Stokes scattering [18]. Due to

thermal energy, a very small quantity of molecules will be excited to higher vibronic states at room temperature. Stokes shifted Raman bands are used for analytical purposes since these bands are more intense than anti-Stokes bands.

3.   Raman Spectroscopy

Raman spectroscopy systems are generally comprised of an excitation source (e.g., laser), receiver, spectrometer, detector and computer. Laser sources stimulate the Raman process, fiber optics, and a microscope or a telescope collects the Raman signals. A laser rejection filter is typically used to reject the laser line (i.e., Rayleigh scattered light) and a spectrometer disperses light along the focal plane of a detector, such as a charge-coupled device (CCD).
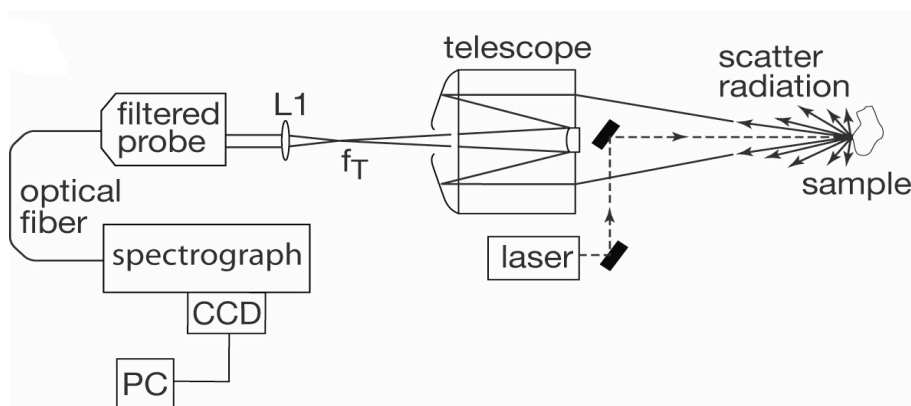
Figure 4.   Illustration of a fiber-optic coupled standoff Raman detection system (From: [19]). The laser beam is coaxial to the telescope field of view. L1 is a collimating lens and f_T is the f-number of the telescope.

Raman spectroscopy is useful for solids, liquids, and gas phase measurements and is currently a widely used analytical technique [18]. There are many analogs between Raman spectroscopy and infrared spectroscopy. The unique absorption bands observed in infrared and Raman spectroscopy both correspond to molecular vibrations, although Raman spectroscopy indirectly probes molecular vibrations. These vibrations can be mapped directly to in- and out-of-plane stretches and vibrations of molecular bonds, which are excited at characteristic frequencies. Since molecular vibrations are sensitive to the local chemical environment surrounding the bond, the infrared and Raman spectra forms a unique molecular "fingerprint" that can be exploited.

Raman Band	Frequency (cm^{-1})	Band Strength
CH_3 symmetric stretch	2862-2882	Very strong
C—C stretch	1040-1100	Strong
$R-NO_2$ asymmetric stretch	1530 – 1600	medium – weak
$R-NO_2$ symmetric stretch	1310-1397	very strong
Aromatic rings	1600	very strong

Table 1.   Table of select vibrational frequencies important in the analysis of high explosives (After: [17]).

Raman and infrared spectroscopy measurements are often used to identify unknown molecules by comparing the unique spectrum of an unknown to molecular databases and vibrational correlation charts. While infrared spectroscopy is an absorption phenomenon, the Raman effect is observed by the scattering of light.   Raman spectroscopy is a weak phenomenon, as previously discussed, and can suffer from fluorescence interference due in part to the sample, the sample matrix/substrate, or due to laser-induced sample degradation.

Anti-Stokes lines are much weaker than Stokes lines by a factor of $e^{-\hbar\omega/kT}$, where $\hbar$ is the reduced Planck constant, ω is the angular frequency, k is Boltzmann's constant, and T is temperature in Kelvin. Thus, anti-Stoke lines are normally omitted in published Raman spectra unless special anti-Stokes techniques are being used.

Figure 5 shows a sample Raman spectrum illustrating Rayleigh, Stokes, and anti-Stokes scattering. The y-axis is the Raman signal intensity and the x-axis is typically presented as the Raman shift in wavenumbers (cm^{-1}).
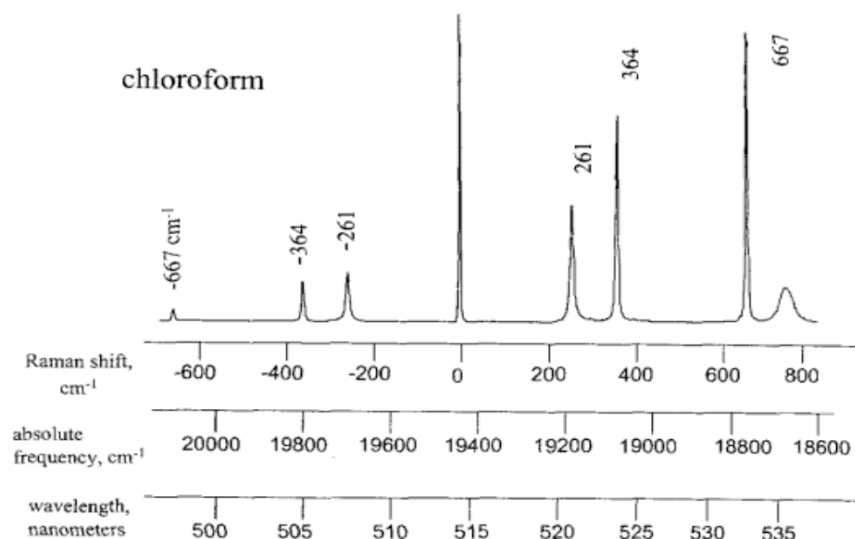
Figure 5.   Raman spectra of chloroform ($CHCl_3$) obtained using a 514.5 nm excitation laser (From: [17]). Note that the Anti-Stokes peaks (left side of the spectrum) are much weaker than those obtained from Stokes processes (right side). The strong center Rayleigh band is blocked in typical measurements so the weak Raman signal is not swamped by the Rayleigh scattered light.

B.   ENHANCING RAMAN MEASUREMENTS

1.   Raman Frequency Dependence

One of the practical beneficial aspects of Raman spectroscopy is that a spectrum acquired using a laser source at 1064 nm will be the same as spectra acquired at other wavelengths (Note: the transmission function of different Raman systems vary, often resulting in Raman spectra having band intensity differences for identical samples acquired with different systems; in addition Raman differences may be due to the v^4 scattering dependence).   While the Raman fingerprint band locations are nearly wavelength independent of the frequency of the excitation laser, the intensity of a normal Raman signal is inversely proportional fourth power of the frequency of the excitation source. This frequency dependence is evident in the following equation:

19

$$I = Kl\alpha^2 v^4$$

$$= K'l\alpha^2 \left(\frac{1}{\lambda}\right)^4 , \qquad (3.1)$$

where I is the scattered signal intensity, K and K' are composite constants, l is the laser power, α is the polarizability of the electrons in the analyte, and v and λ are the frequency and wavelength of the incident light. For normal (non-resonance) Raman, the polarizability of the molecule is constant, but this term becomes very important for the resonance Raman processes.

The first standoff Raman measurement of high explosives was obtained using a 532 nm laser source [19]. It follows from taking the ratio of Equation 3.1 at two different wavelengths that shifting to a 229 nm laser source should achieve an immediate 29-fold improvement in the signal intensity. Raman spectroscopic measurements, acquired with excitation wavelengths in the near-infrared (NIR), are commonly performed to reduce contributions from sample fluorescence, which is more likely to occur when using excitation wavelengths in the visible portion of the electromagnetic spectrum. But a Raman measurement made at 229 nm should theoretically have a 138-fold advantage to that made using a 785 nm source, assuming all other factors are the same. However, Raman spectroscopy is not one-dimensional; other notable factors to consider include sample fluorescence, absorption, potential resonance enhancements, matrix interferences, and particularly laser-induced sample degradation.

2. Resonance Raman

In addition to frequency enhancements gained from using a UV laser to make Raman spectroscopy measurements, additional gains are achieved when the energy of the laser is close to the energy of a strong electronic transition of the analyte molecule. This enhancement is known as resonance Raman scattering and can provide enhancements of three to four orders of magnitude [18].
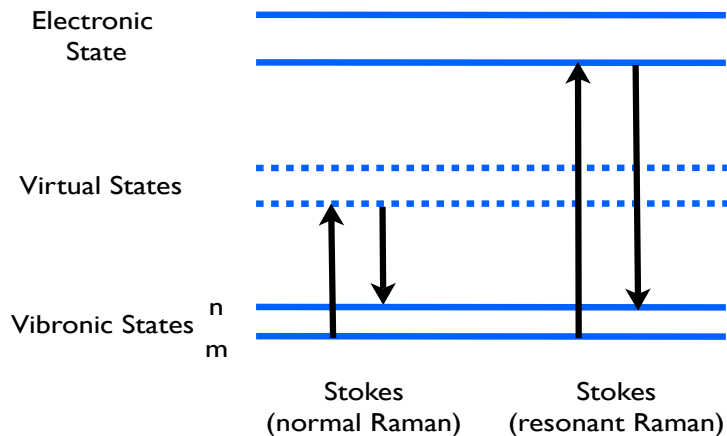
Figure 6.   Illustration of the principal difference between normal Raman and resonance Raman. The virtual state in normal Raman spectroscopy is not necessarily a true quantum state of the molecule, like those participating in resonance Raman.

In theory, resonance Raman enhancements are most pronounced when the excitation wavelength is chosen to coincide with a wavelength (λ_{max}) where the molar absorptivity of the analyte is maximum (ε_{max}); this is an electronic transition within the molecule.   Resonance enhancements associated with a given electronic transition increases proportional to the square of the molar absorptivity [20].

Analysis of the Kramer Heisenberg Dirac (KHD) expression provides mathematical insight into the means of enhancing the resonance Raman effect [18]. The KHD expression is

$$\left(\alpha_{\rho\sigma}\right)_{GF} = k\sum_{I}\left(\frac{\langle F|r_{\rho}|I\rangle\langle I|r_{\sigma}|G\rangle}{\omega_{GI} - \omega_{L} - i\Gamma_{I}} + \frac{\langle I|r_{\rho}|G\rangle\langle F|r_{\sigma}|I\rangle}{\omega_{IF} + \omega_{L} - i\Gamma_{I}}\right), \tag{3.2}$$

where α is the molecular polarizability, ρ is the direction of the incident polarization, σ is direction of the scattered polarization, G is the ground vibronic state, I is an excited vibronic state, F is final vibronic state of Raman scattering, r_{σ} is the dipole operator, ω_{L} is the frequency of the laser/incident radiation, ω_{GI} and ω_{IF} are difference angular frequencies between the ground state and an excited vibronic state and the excited state and final state respectively, and $i\Gamma_{I}$ is small factor relating to the lifetime of the virtual

21

excited state called the phenomenological damping constant [18]. Use of Dirac's "bra-ket" notation makes this summation over all vibronic states look deceptively simple considering that each numerator consists of two triple integrals multiplied by one another. Fortunately this equation can be easily dissected [18]. The summation occurs over all vibronic states, although typically only the first few excited states are primarily involved. The numerators of the KHD expression mathematically express the nature of the Raman scattering depicted in Figures 3 and 6. Since there is no reason why this process should have to start in the ground state, there are two terms required to account for both Stokes and anti-Stokes scattering. The simplicity in analyzing this equation comes from analysis of the denominator, commonly called the resonance denominator. The energy of the $i\Gamma_I$ term, which is a term added to account for the lifetime of the excited state, is small compared to ω_{GI} and ω_L. If the laser wavelength is chosen to correspond closely to the energy required to excite the molecule into an electronic transition, the denominator for Stokes scattering becomes very small (approximately $i\Gamma_I$, which itself is small), and the resulting value of the evaluated equation grows significantly accounting for the resonance effects. Not all Raman bands will be enhanced over normal Raman processes [23]. The KHD equation is useful to gain physical insight concerning the Raman resonance effect, but since the observed perturbations are large, quantum perturbation theory is not valid. For a detailed theory of Raman resonance using a vibronic coupling model see Ref [22].

Since most samples absorb in the UV wavelengths, self-absorption of the Raman scattering signal factor complicates resonance Raman measurements over normal Raman techniques [21]. Additionally, this absorption can cause photodegradation of the analyte. These effects can mitigate some of the potential benefits of resonance Raman spectroscopy.

C.   NOISE

1.   Shot Noise

Spectrometers that use a cooled CCD or intensified CCD (ICCD) are normally sample shot noise limited; the dark noise is normally very small in these detectors [23].

Shot noise is a fundamental phenomenon that arises from the random nature of emission of light in excitation processes. Shot noise will always be present in Raman measurements, but in standoff Raman measurements the background noise will typically dominate over the fundamental shot noise limits of the measurement.

2.   Background Effects

Background noise is any photon detected by the system that does not emanate from the analyte. Background effects are typically significant noise contributors in Raman measurements. When concomitant species in a sample matrix have Raman shifts near the analyte peaks, peaks can get convolved and obscured. The simplest example of this is the atmospheric O_2 Raman band that can either convolve or strongly dominate over the band that arises from an asymmetric stretch R-NO_2 in solid explosive samples.

When the excitation laser induces fluorescence of the analyte or in other species in the sample matrix, the very broad fluorescence peak can significantly raise the noise floor and in some cases completely obscure analyte peaks. Unlike the specific 'fingerprint' Raman selection rules, fluorescence selection rules are less specific and typically do not provide as useful chemical information for qualitative identification of a molecule, particularly in mixtures of samples. If fluorescence effects are prevalent there are a number of techniques that can be employed including changing the excitation wavelength. Selecting a near infrared (NIR) laser or using a laser below 240 nm can significantly reduce or eliminate background fluorescence [21].

3.   Signal-to-Noise Ratio

The Raman signal intensity divided by the root-mean-square noise signal is the typical definition of the signal-to-noise ratio (SNR or S/N) [5]. This ratio is a key indicator of the quality of the Raman measurement, and typically the signal peak becomes visually imperceptible over noise signals when the SNR falls below a value of two or three [24]. In Raman spectroscopy applications where background signals are relatively consistent, the S/N ratio can typically be increased by increasing source

irradiance, exciting the Raman process using lower frequencies of laser light, co-addition of a number of collected spectra, and using longer interrogation times [5, 24].

IV.   PREVIOUS RAMAN RESEARCH

A.   RAMAN DETECTION OF EXPLOSIVES

1.   Raman as a Forensic Tool

Raman spectroscopy began to flourish in the 1970s with the increased availability of lasers. During this period, IR and Raman spectra of several explosives were published and the fundamental molecular vibrations were assigned to observed frequency bands [25, 26]. Later, in the 1990s, Raman spectroscopy found a new application in forensic science when it was applied to the detection of explosives [27, 28, 29]. While validated as a new analytical method to detect explosives, due to the unavailability of Raman spectrometers in most analytical laboratories in the 1990s, it became more widely used to confirm the presence of explosives after other analytical tests had been used to detect their presence. Other forensic applications grew out of these efforts including in-situ analysis with portable instruments and even the analysis of explosive residues on fingerprints [18].

2.   Resonance Raman Spectroscopy of Explosives

In the late-70s and early 80s, the application of resonance Raman in physical chemistry and analytical chemistry fields began to emerge [20]. Sands et al. first observed UV resonance Raman spectra of impure explosives and narcotics using the 244 nm line from a frequency-doubled Argon ion (Ar^+) laser-based Raman microscopy system [30]. Resonance enhancements greater than normal frequency (v^4) related enhancements were observed but not quantified. In some cases, simplifications of the Raman spectra were also observed as weaker bands were obscured.

Nagli et al. determined the absolute Raman cross sections of TATP, PETN, RDX and TNT explosives from 620 to 248 nm at a constant flux of $2.5 \cdot 10^{24}$ quanta s^{-1} cm^{-2} using KNO_3 (potassium nitrate) powder as an internal standard [31]. They reported normalized UV Raman signals were 100-200 times stronger at 248 nm when compared to

measurements made at 532 nm. Their study also included reported strong fluorescence of many background materials at 532 and 785 nm excitation with a significant reduction in background fluorescence at 248 nm.

Comanescu et al. recently published a comprehensive study on the resonance Raman spectra of TNT, RDX, HMX, and PETN using 40 UV wavelengths from 210 to 280 nm using a 90° collection geometry [32]. This study includes tables that detail excitation wavelengths that produced the strongest Raman bands for HE samples in acetonitrile solutions. The strongest Raman bands tend to be the symmetric NO_2 stretch and the symmetric phenyl stretch, which is consistent with Raman selection rules.

B.   STANDOFF RAMAN

In 1992, Angel et al. demonstrated standoff Raman detection of ferrocyanide at distances of 20 m using 488 nm and 809 nm continuous wave (CW) lasers, a 40 mm collection optic, spectrograph, and a liquid-nitrogen cooled CCD [33].

In 2000, Ray et al. at Brookhaven National Laboratory developed a UV Raman lidar system for the standoff detection of contaminants at distances of 30 m or less using a pulsed Nd:YAG laser operating at 266 nm with an average intensity of 200 mW/cm^3, six inch Newtonian telescope, spectrograph, and CCD camera [34]. In the article, Ray and coworkers used cyclohexane, acetonitrile, and Teflon® for his proof of concept.

In 2005, Carter at Lawrence Livermore National Laboratory, in cooperation with Angel and other researchers at the University of South Carolina, performed the first Raman standoff detection measurements of high explosives in a silica matrix [19]. Using a pulsed 10 Hz Nd:YAG laser at 532 nm, an 8 in Schmidt–Cassegrain telescope, spectrograph and a gated ICCD camera, various explosive samples were detected at standoff distances up to 50 meters. This work also included a power density study which demonstrated linear Raman intensities up to ~3 x 10^6 W/cm^2. Additionally, in some HE samples photodecomposition or other signal degrading effects were observed.

Sharma and collaborators at the University of Hawaii published their standoff Raman results just a few months following Carter's work. Sharma measured milligram (mg) quantities of explosives samples at 10 m using a pulsed Nd:YAG laser (532 nm, 10 Hz) with a Cassegrain-Maksukov telescope (f/15) and ICCD [35].

Gaft and Nagli recently reported sub-microgram (sub-μg) detection limits of explosives at distances up to 30 m using a gated standoff Raman system at distances of 30 m [36].

THIS PAGE INTENTIONALLY LEFT BLANK

V. METHOD

A. RAMAN CROSS SECTIONS

The intensity of a Raman line can be expressed in two different ways: (1) from a purely theoretical or (2) an experimental viewpoint. In the former case, the total Raman scattering cross section, σ, for the vibrational transition from n←m for an isolated molecule described in Ref. [37] as follows:

$$\sigma_{mn} = \frac{I_{mn}}{I_0},\qquad (5.1)$$

where I_{mn} is the Raman intensity over 4π steradians of the vibrational transition n←m ratioed to the incident excitation intensity, I_o. The above expression is a function of the incident and Raman mode frequencies, the degeneracy and thermal occupancy of state m, and the Raman polarizability tensor [37]. In the latter case, the experimentally observed Raman line intensity is given as the following expression adapted from Ref. [37].

$$I_{mn} = I_0 \cdot N \cdot D \cdot K \cdot \sigma_R,\qquad (5.2)$$

where I_{mn} is related to the molecular density (N) in molecules cm^{-3}, incident excitation intensity (I_o), sample pathlength (D – based on incident beam and Raman scattered attenuation), several variables for collection and detection of the scattered light (K), and the Raman scattering cross section (σ_{mn}).

An absolute differential Raman cross section (σ_R), a differential scattering probability per unit of solid angle, can readily be calculated using internal standards and by comparing the relative Raman cross section to a known absolute differential Raman cross section. This is shown in the following equation, which was adapted using acetonitrile as the internal standard [37, 38]:

$$\left(\sigma_R\right)_{v_A} = \left(\sigma_R\right)_{919}\left(\frac{I_{v_A}}{I_{919}}\right)\left[\frac{v_0(v_0-919)^3}{v_0(v_0-v_A)^3}\right]\left(\frac{C_{ACN}}{C_A}\right)L,\qquad (5.3)$$

29

where $(\sigma_R)_{v_A}$ and $(\sigma_R)_{919}$ are the absolute differential Raman cross sections of the analyte and acetonitrile reference sample respectively, I_{v_A} and I_{919} are the integrated scattering intensities of the analyte and acetonitrile bands respectively, v_0 is the frequency of the incident excitation laser, 919 is the observed Raman shift of the reference acetonitrile peak in cm^{-1}, v_A is the frequency of the observed analyte band Raman shift in cm^{-1}, and L is a dimensionless term that factors in the change in local field effects differences between gas samples and solutions [47, 48, 49]. L can be described using the index of refraction of the solution using the following expression [37, 38, 45, 48, 49]:

$$L = \left(\frac{n_{v_0 - v_{mn}}}{n_{v_0}} \right) \left(n_{v_0 - v_{mn}}^2 + 2 \right)^2 \left(n_{v_0}^2 + 2 \right)^2 / 81$$

$$\approx \left(\frac{n^2 + 2}{3} \right)^4 , \tag{5.4}$$

where the index of refraction of the solution (n) is assumed to approximately equal the indices of refraction evaluated at the analyte band frequency ($n_{v_0 - v_{mn}}$) and the frequency of the incident laser (n_{v_0}).

B.   RAMAN ENHANCEMENTS IN SOLUTION

Acetonitrile was chosen as an internal standard for this enhancement study for two reasons: it is an effective solvent for high explosives and it is a useful internal standard to quantify resonance enhancements. The 919 cm^{-1} C-C stretch in acetonitrile was shown by Dudik et al. [37] to be solely dependent on the well-known υ^4 Raman frequency dependence since it does not display any resonance or pre-resonance enhancements. For this reason, Raman enhancements can be readily calculated by making Raman cross section calculations using the internal standard.

To develop an expression for resonance enhancements, Equation 5.3 is evaluated at pre-resonance/resonance Raman conditions (UV excitation denoted by subscript UV)

30

and ratioed to the same equation evaluated under normal (i.e., non-resonance) Raman conditions (NIR or visible excitation with the subscript NIR). This yields:

$$\frac{\left(\sigma_R\right)_{v_A}}{\left(\sigma_R\right)_{v_A}} = \frac{\left[\left(\sigma_R\right)_{919}\left(\dfrac{I_{v_A}}{I_{919}}\right)\left[\dfrac{v_0(v_0-919)^3}{v_0(v_0-v_A)^3}\right]\left(\dfrac{C_{ACN}}{C_A}\right)L\right]_{v_{UV}}}{\left[\left(\sigma_R\right)_{919}\left(\dfrac{I_{v_A}}{I_{919}}\right)\left[\dfrac{v_0(v_0-919)^3}{v_0(v_0-v_A)^3}\right]\left(\dfrac{C_{ACN}}{C_A}\right)L\right]_{v_{NIR}}}. \qquad (5.5)$$

Since $\left(\sigma_R\right)_{919}$ approximately varies only with the v^4 frequency enhancements,

$$\frac{\left[\left(\sigma_R\right)_{919}\right]_{v_{UV}}}{\left[\left(\sigma_R\right)_{919}\right]_{v_{NIR}}} \approx \left[\frac{v_{UV}}{v_{NIR}}\right]^4 \qquad (5.6)$$

Equation 5.5 can be rearranged to give an expression for the resonance Raman enhancement of UV measurement relative to the normal Raman measurement that is independent of the v^4 Raman frequency enhancements:

$$\begin{aligned}
E_{SOLN} &\equiv \frac{\left[\left(\sigma_R\right)_A / \left(\sigma_R\right)_{919}\right]_{v_{UV}}}{\left[\left(\sigma_R\right)_A / \left(\sigma_R\right)_{919}\right]_{v_{NIR}}} \\[2mm]
&\approx \frac{\left[\left(\dfrac{I_{v_A}}{I_{919}}\right)\left[\dfrac{(v_0-919)^3}{(v_0-v_A)^3}\right]\left(\dfrac{1}{C_A}\right)\right]_{v_{UV}}}{\left[\left(\dfrac{I_{v_A}}{I_{919}}\right)\left[\dfrac{(v_0-919)^3}{(v_0-v_A)^3}\right]\dfrac{1}{C_A}\right]_{v_{NIR}}}.
\end{aligned} \qquad (5.7)$$

This step assumes that the index of refraction of the solution used in the NIR measurements is approximately equal to the index of refraction used in the UV measurements to cancel the local field terms (*L*). The index of refraction can be expressed as a function of concentration and wavelength [39]. The index of refraction is only weakly wavelength dependent and the concentration of all samples is approximately 19 mol L^{-1} (M) acetonitrile, so any error introduced from the local field term will be small. Additionally, since the concentration of acetonitrile is nearly the same for UV and NIR measurements, the C_{ACN} terms cancelled.

The Beer-Lambert law describes the transmission of light through a sample:

$$T = \frac{I}{I_0} = 10^{-\varepsilon bc}, \tag{5.8}$$

where T is the transmission, I_0 and I are the light intensities before and after entering the sample, ε is the molar absorptivity (L mol⁻¹cm⁻¹), b is the path length (cm), and c is the concentration (mol L⁻¹) [5]. The transmission of the sample may also vary across the Raman spectrum, and this effect is more pronounced in UVRR analysis. To derive Equation 5.3, Dudik et al. assumed that the transmission of the solution at the analyte and reference bands was approximately the same; however, it is necessary to reintroduce the transmission term since most explosive samples strongly absorb UV radiation. This leads to the final version of the Raman enhancement formula for solutions (E_{SOLN}):

$$E_{SOLN} \equiv \frac{\left[(\sigma_R)_A / (\sigma_R)_{919}\right]_{v_{UV}}}{\left[(\sigma_R)_A / (\sigma_R)_{919}\right]_{v_{NIR}}}$$

$$\approx \frac{\left[\left(\frac{I_{v_A}}{I_{919}}\right)\left[\frac{(v_0 - 919)^3}{(v_0 - v_A)^3}\right]\left(\frac{1}{C_A}\right)\left(\frac{T_{919}}{T_{v_A}}\right)\right]_{v_{UV}}}{\left[\left(\frac{I_{v_A}}{I_{919}}\right)\left[\frac{(v_0 - 919)^3}{(v_0 - v_A)^3}\right]\left(\frac{1}{C_A}\right)\left(\frac{T_{919}}{T_{v_A}}\right)\right]_{v_{NIR}}}. \tag{5.9}$$

After Raman and UV-Visible (UV-Vis) spectra are collected and analyzed, Equation 5.9 is used to calculate the excitation wavelength dependent resonance Raman enhancements for individual Raman bands.

C.   RAMAN ENHANCEMENTS IN SOLIDS

Since many high explosive solids highly absorb UV light, their molar absorptivity can be over 10^4 L mol⁻¹cm⁻¹. When the concentration, molar absorptivity, and concentration of a sample is fixed, Equation 5.8 can be used to calculate the maximum penetration depth of UV laser light into a sample. This depth is typically of the order of a tenth of a micron to microns for explosive samples in UVRR measurements. If the photon is Raman scattered before being absorbed by the sample, the scattered Raman

signal can be self-absorbed before getting out of the sample (see Figure 7). Using Equation 5.8 and assuming no atmospheric attenuation, the strength of the laser at the point of Raman scattering is

$$I = I_0 10^{-\varepsilon_0 bc} , \tag{5.10}$$

where ε_0 is the molar absorptivity of the sample at the wavelength of the incident laser, and b is the path length through the solid to the scatterer. Applying the Beer-Lambert law to the Raman signal out of the solid sample (I_{mn}) at a particular path length, we now have

$$\begin{aligned} I_{mn} &\propto I_0 \cdot 10^{-cb(\varepsilon_0 + \varepsilon_R)} \\ &= I_0 \cdot e^{-2.304 cb(\varepsilon_0 + \varepsilon_R)} , \end{aligned} \tag{5.11}$$

where ε_R is the molar absorptivity of the sample at the wavelength of Raman signal and the path length from the scatterer back out of the sample is $\sim b$ for a 180° collection geometry.
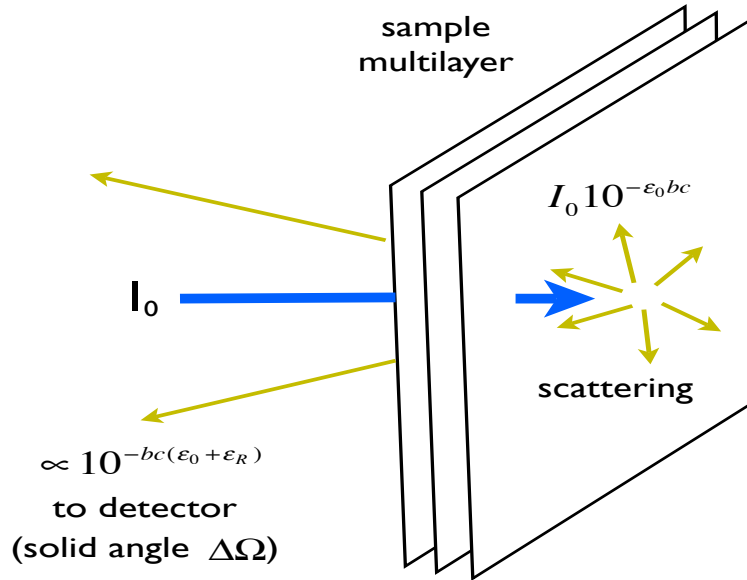
Figure 7.   Difficulties arise in UVRR due to the attenuation of the laser into the sample and the self-absorption of the Raman signal out of the sample.

The total magnitude of Raman signal over all path lengths for a given sample depth (D) is also proportional to the differential cross section of the molecule (σ_R) in $cm^2\ sr^{-1}$

(steradian), molecular density (N) in molecules cm^{-3}, and K describes the variables for collection and detection of the scattered light [40]:

$$I_{mn} = I_0 \cdot \sigma_R \cdot K \cdot N \int_0^D e^{-2.303bc(\varepsilon_0 + \varepsilon_R)} db . \qquad (5.12)$$

The physical interpretation of the integral in Equation 5.12 is the penetration depth of the sample, where I_{mn} is reduced to a value of 1/e (~0.368), which only equals the sample depth when molecular absorptivity is negligible [40]. Taking the ratio of UV and NIR measurements using Equations 5.9 and 5.12 is a step closer to deriving a formula for Raman enhancements in solids (E_S):

$$E_S \propto \frac{[\sigma_R]_{UV}}{[\sigma_R]_{NIR}} \frac{\left[\int_0^D e^{-2.303bc(\varepsilon_0 + \varepsilon_R)} db \right]_{UV}}{\left[\int_0^D e^{-2.303bc(\varepsilon_0 + \varepsilon_R)} db \right]_{NIR}} . \qquad (5.13)$$

Additionally, it follows from Equations 5.6 and 5.7 that:

$$E_{SOLN} \approx \frac{[\sigma_R]_{UV}}{[\sigma_R]_{NIR}} \left(\frac{\lambda_{NIR}}{\lambda_{UV}} \right)^4 . \qquad (5.14)$$

This leads to the final relationship for comparing observed Raman enhancements in solution to solid samples:

$$E_S \approx E_{SOLN} \frac{L_S}{L_{SOLN}} \left(\frac{\lambda_{NIR}}{\lambda_{UV}} \right)^4 \frac{\left[\int_0^D e^{-2.303bc(\varepsilon_0 + \varepsilon_R)} db \right]_{UV}}{\left[\int_0^D e^{-2.303bc(\varepsilon_0 + \varepsilon_R)} db \right]_{NIR}} , \qquad (5.15)$$

where L_S and L_{SOLN} are the local field effect terms evaluated for solid and solution samples respectively. In Equation 5.14, ε_0 and ε_R represent the combined absorption and scattering coefficient for the solid (e.g., powder or polycrystalline) sample. In this final step a correction term for L, which is expected to be stronger in solids than in solutions, was applied. L_S and L_{SOLN} can be calculated using the wavelength dependent indices of refraction, some of which are available in the literature, e.g. see Ref. [40]. Using Equation 5.14, the resonance Raman enhancements from solution measurements can now be analyzed to estimate the magnitude of total enhancements (i.e., resonance Raman

enhancement multiplied by the frequency dependent enhancement and local field enhancement) of UVRR measurements in solid samples.

Finally, if these measurements are to be applied to standoff distances, the atmospheric attenuation of the laser and Raman signal in air over a standoff distance ($I_{standoff}$) must be considered:

$$I_{standoff} \propto I_{mn} 10^{-2d \sum_{i} \varepsilon_i c_i},$$ (5.16)

where d is the standoff distance and ε_i and c_i are the molar absorptivity and concentrations of individual components of the atmosphere respectively. For UV wavelengths, ozone (O_3) has been reported as the principle absorbing species [14].

THIS PAGE INTENTIONALLY LEFT BLANK

VI. EXPERIMENTAL TECHNIQUES

A. OBJECTIVES

The goal of this research was to quantitatively determine resonance Raman enhancements in the absence of the frequency dependent enhancements for select high explosive (HE) materials by contrasting Raman measurements at 785, 244, and 229 nm excitation wavelengths using an internal standard. The internal standard (acetonitrile) exhibits no resonance or pre-resonance Raman effects and did not overly convolve the analyte Raman peaks. The experimental conditions between ultraviolet resonance Raman (UVRR) and near-infrared (NIR) Raman systems were matched to the greatest extent possible given experimental constraints, and the use of an internal standard allows quantitative comparison between measurements. Using this technique it is possible to determine the benefits of UV excited Raman compared to normal Raman techniques for the standoff detection of high explosives.

B. EXPERIMENTAL SUMMARY

UV-visible (UV-Vis) absorption measurements were performed to select solution concentrations for UVRR analysis and to collect required transmission data for Raman enhancement calculations and corrections. Sample solutions at a single fixed dilute solution (varying from 2.2 to 9.27 mM for different analytes) were placed in a 1.00 mm path length (sealable) quartz cell for UVRR analysis. UVRR measurements of sample solutions were made for three to five sample replicates at five different laser powers settings for each replicate ranging from 20 μW to 2.2 mW. The laser was rastered across the cell during the 180-second analysis time to prevent or minimize localized heating and photodegradation effects that could negatively influence the measurement. Three replicates of one fixed sample concentration between 100 to 150 mM were used for NIR Raman measurements at 50 mW. The higher concentration was necessary since the analyte Raman band intensities were weaker for NIR excitation; NIR excitation provides no resonance enhancements effects and Raman scattering power goes as v^4. The laser

37

power for NIR measurements did not produce any observable degradation of any samples; Raman intensity measurements over 6 minutes for fixed spot were found to be highly reproducible.

Approximately 10 mg quantities were used for Raman analysis of solid samples. Samples were placed on glass slides for UVRR and NIR Raman analysis for 180 seconds. The UV laser was rastered across the solid samples for UVRR analysis to prevent photodegradation effects and heating. Raman spectra were analyzed to determine integrated peak intensities (area under the Raman bands) to perform enhancement calculations.

The use of the internal standard greatly simplifies the comparison of measurements made on separate Raman systems. Taking the ratio of the analyte and reference bands in Equation 5.8 negates the differing power settings between the systems, differing sampling volumes, differing detector pixel sizes, differing system f-numbers, sample absorbance of the excitation laser in the sample, and other differences that cannot easily controlled experimentally. The spectral bandpass of the two Raman systems and sample analysis times were matched for added measure.

C.   EQUIPMENT

Two separate Raman systems were used at Lawrence Livermore National Laboratory to collect the data for this thesis. Measurements were collected using ultraviolet and near infrared excitation for resonance and normal Raman spectroscopy. All laser power measurements were made using an Ophir NOVA II power meter (Bionetics, St. Laurent, QC, Canada).

Sample absorbances were measured using a Cary 300 Bio UV-Vis spectrophotometer (Varian, Inc., Palo Alto, CA, USA) and baseline corrected using acetonitrile.

1. NIR (785 nm) Raman System

This Raman system consisted of an Invictus 785-nm NIR Laser (Kaiser Optical Systems, Ann Arbor, MI, USA), Mark II Filtered Probe Head utilizing holographic optics (Kaiser Optical Systems, Ann Arbor, MI, USA), f/4 spectrograph (Chromex, Model 250IS/RF, Albuquerque, NM, USA), liquid-nitrogen-cooled CCD system (1340×400 pixels, Princeton Instruments, Trenton NJ, USA). The Raman signal intensity captured in the vertical channels of the ICCD was binned to a single channel. The spectrometer and optical fiber probe had focal ratios of f/4 and f /2, respectively, resulting in some Fresnel losses. The spectral bandpass of the spectrometer was 12 cm^{-1} for a 149 μm slit width and the 600 grooves / mm grating.
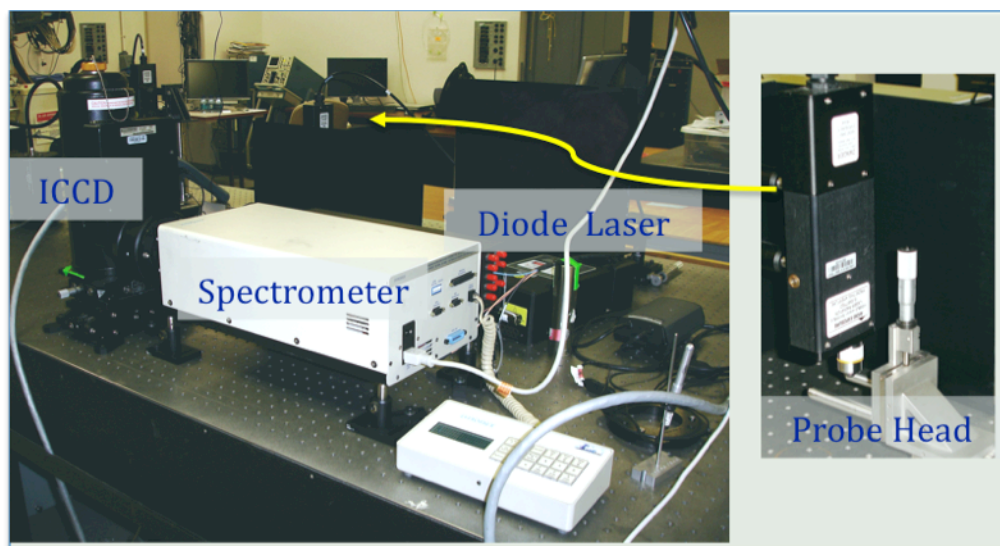
Figure 8.   Picture of the NIR Raman System showing the placement of key components.

This system was calibrated using a 50% v/v (volume / volume) solution of toluene / acetonitrile (see Appendix A). Peaks locations on the camera's pixels were matched to known Raman shift locations in wavenumbers for the reference standard using a quadratic peak-fitting model using WinSpec 32 software.

2. UV Raman Microscopy System

This device consists of a water-cooled Argon ion laser (Lexel, Model 85-SHG, Fremont, CA, USA), microscope (Leica DMLM, Leica Microsystems, Wetzlar, Germany), ICCD (2048 x 512 pixels, Princeton Instruments, Trenton, NJ, USA), and f/5.7 spectrograph (Model PI SpectraPro 2500i, Princeton Instruments, Trenton NJ, USA). The spectral bandpass of the spectrometer was 12 cm^{-1} for a 100 μm spectrometer slit width and the 2400 grating / mm grating. The microscope translation stage was equipped with an electronic joystick controller for manual x- and y-axis rastering of the laser across the sample.
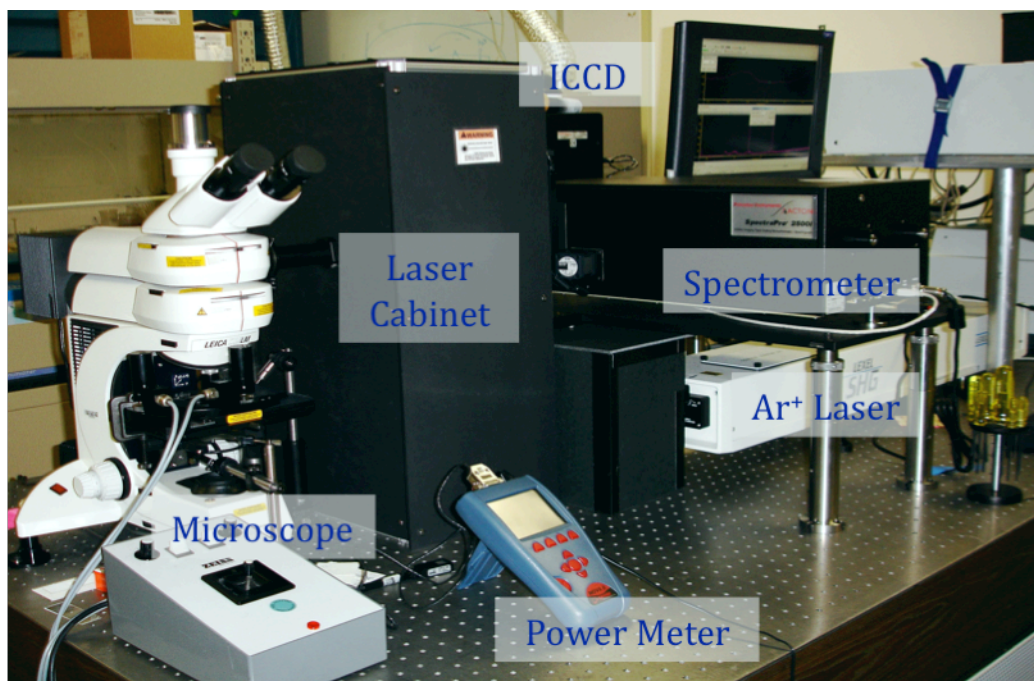
Figure 9.   Photo of the UV Raman Microscopy System highlighting the system's key components.

The UV laser system was initially setup for 244 nm (frequency doubled 488.0 nm line) excitation with a maximum power at the sample of 2.2 mW. The laser was later modified to emit at 229 nm by frequency doubling the 457.9 nm line. The addition of new optics suitable for UV wavelengths, including the addition of two Pellin-Broca prisms to remove Ar ion plasma lines, reduced usable power to 1.0 mW at the sample for 229 nm measurements.

The manufacturer's wavelength calibration was used for all UVRR system measurements at 244nm excitation. For 229 nm measurements it was necessary to calibrate using cyclohexane as a Raman shift standard (see Appendix A).

D.   SAMPLES AND SAMPLE PREPARATION

Toluene from EMD Chemicals Inc. (Darmstadt, Germany) and spectroscopic grade acetonitrile from Riedel-de Haën Laborchemikalien GmbH & Co. (Hannover, Germany) was used as received. Acetonitrile was used for all Raman solution preparations. Cyclohexane for select UV-Vis spectrometer measurements was obtained from Sigma Aldrich (St. Louis, MO, USA).

2,4-DNT (2,4-dinitrotoluene); 2,3-DNT (2,3-dinitrotoluene); 3,4-DNT (3,4-dinitrotoluene); 2,6-DNT (2,6-dinitrotoluene); PNT (p-nitrotoluene), 2,4,6-TNT (2,4,6-trinitrotoluene), HMX (1,3,5,7-tetranitro-1,3,5,7-tetrazocane), RDX (1,3,5-trinitroperhydro-1,3,5-triazine), Composition B (63% RDX, 36% TNT and 1% paraffin wax), PETN (pentaerythritol tetranitrate), ANFO (ammonium nitrate / fuel oil), and TATB (1,3,5-triamino-2,4,6-trinitrobenzene) were high purity samples provided by LLNL's High Explosives Applications Facility (HEAF) and Forensic Science Center.

All reagents, with the exception PETN, were used without further purification. PETN solutions were centrifuged at 6000 rpm for 12 minutes to remove scattering particulates found in 150 and 9 mM solutions. PETN is typically coated with polyethylene to reduce the sensitivity of the explosive, and UV Raman analysis of the PETN impurity insoluble in acetonitrile was consistent with polyethylene and other similar molecules.

Solid samples (approximately 10 mg quantities) were transferred from storage vials to glass slides (Gold Seal, Thermo Fisher Scientific Inc., Waltham, MA, USA) for spectral analysis.

The same UV/Vis cuvette (1.00 mm path length, QS grade, Hellma, Forest Hills, NY, USA) was used for all solution spectral measurements. The cuvette was triple rinsed

with acetonitrile, air dried, and rinsed with the new sample prior to introducing a new sample for measurement.

E.   DATA HANDLING

WinSpec 32 spectroscopy software (Princeton Instruments, Trenton, NJ, USA) was used for data acquisition and system calibration. Data files were converted to ASCII files and plotted using IGOR Pro 6 (WaveMetrics, Portland, OR, USA). Data from UV Raman measurements were recorded in wavelength (nm) and converted to Raman shift in wavenumbers (cm^{-1}) using a simple MATLAB (The Math Works, Natick, MA, USA) program.

The goal of making Raman band area calculations was to use an accurate and simple program that could be used by most analytical laboratories without requiring special software. MATLAB programs (see Appendix B for source code) were used to baseline the spectra between two user-selected points, to select the start/end of a Raman peak, and to calculate the area under spectral peaks for subsequent Raman enhancement calculations.   Two versions of the program were utilized: one to be used with deconvolved peaks and another that can be used with peaks that were partially convolved. The latter program calculated half of the peak area of a visible peak and invoked symmetry to calculate the full peak area of the band; a similar method has been reported by Mallard et al. [46]. The use of PeakFit (Aspire Software International, Ashburn, VA, USA) nonlinear curve fitting software was also summarily examined for baselining and deconvolution of the data; however, the Gaussian, Lorentzian and other user-selected data models didn't accurately fit the form of the peaks obtained in this research. The Raman peaks should be mixed Gaussian and Lorentzian functions due to pressure broadening, Doppler sifting, and other instrument response features [41]. PeakFit may still be an effective tool for these calculations, but this research emphasized the developed of MATLAB tools and so the use of Peakfit was abandoned. The accuracy of the MATLAB model was validated using the cumulative area tool in PeakFit, which does not require fitting the peaks to any mathematical models.

VII.   RESULTS

A.   SUMMARY OF RESULTS

1.   Molar Absorptivity and Solvent Effects

Resonance Raman enhancements of PETN; PNT; 2,4-DNT; and 2,4,6-TNT were measured using acetonitrile as both the solvent and internal standard.   In theory, resonance Raman enhancements are most pronounced when the excitation wavelength is chosen to coincide with a wavelength (λ_{max}) where the molar absorptivity of the analyte is maximum (ε_{max}); this is an electronic transition within the molecule.   Resonance enhancement associated with a given electronic transition increases with the square of the molar absorptivity [20].   The molar absorptivity of high explosive samples and select explosive precursors dissolved in acetonitrile were calculated from absorption measurements and are presented in Figure 10.
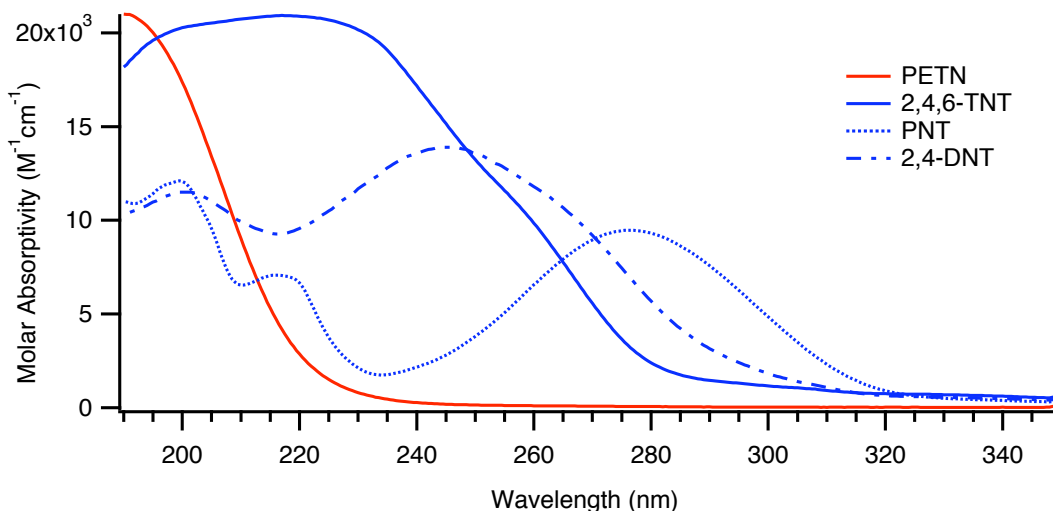
Figure 10.   Calculated molar absorptivities (ε) from absorption measurements of PETN, PNT, 2,4-DNT, and 2,4,6-TNT in acetonitrile. It is interesting to note that the molar absorptivity 2,4,6-TNT > 2,4-DNT > PNT at ε_{max} which corresponds with the increasing number of NO_2 substitutions on the aromatic ring.

The observed ε_{max} results for the nitroaromatic species were compared to literature values and are presented in Table 2.

Analyte	Literature		Observed	
	λ_{max} (nm)	ε_{max} (M^{-1}cm^{-1})	λ_{max} (nm)	ε_{max} (M^{-1}cm^{-1})
PNT	264	10100	276	9470
2,4-DNT	233	15800	245	13900
2,4,6-TNT	224.5	23000	217.5	20900

Table 2.   Calculated and reference maximum molar absorptivities for the primary $\pi \rightarrow \pi^*$ transitions observed at wavelengths >220 nm for PNT; 2,4-DNT; and 2,4,6-TNT in acetonitrile. Reference values for PNT and 2,4-DNT were obtained using n-heptane as a solvent and 2,4,6-TNT was observed in cyclohexane [42].

The results obtained for λ_{max} and ε_{max} for the $\pi \rightarrow \pi^*$ transition (a stable bonding to an unstable anti-bonding orbital) for PNT and 2,4-DNT noticeably differ from the literature values due to solvent effects. These analytes display a bathochromic (red shifting) of the UV-Vis spectra in the polar acetonitrile solvent. The observed bathochromic shifts are consistent with the polar acetonitrile solvent molecules stabilizing (lowering) the excited state relative to the ground state [43]. The bathochromic shift is very noticeable in the following example experimental results of calculated molar absorptivities for 2,4-DNT in polar acetonitrile and non-polar cyclohexane solutions (Figure 11).
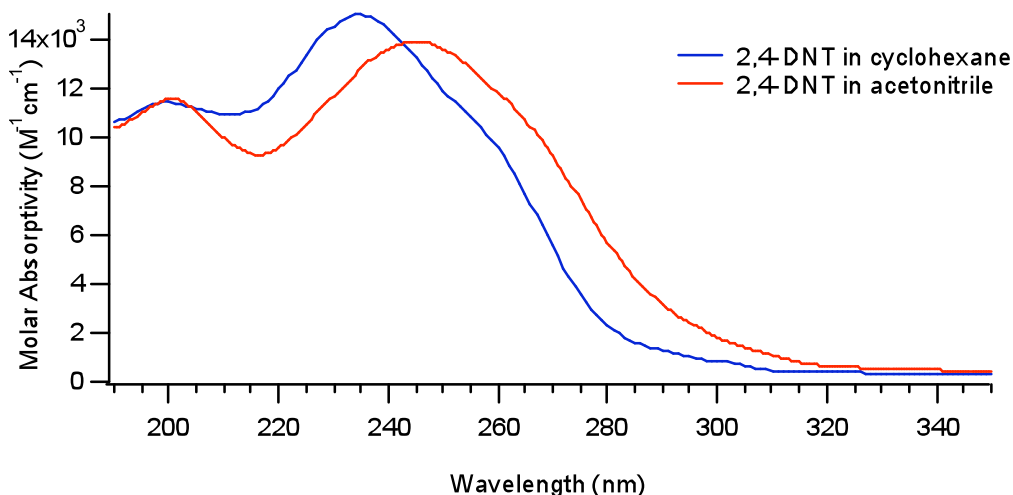
Figure 11.   Calculated molar absorptivities (ε) of 2,4-DNT in acetonitrile and cyclohexane. The use of a polar solvent produces broadening and bathochromic shifting of the peak of the main $\pi \rightarrow \pi^{*}$ transition observed at 234 nm in cyclohexane and 245 nm in acetonitrile. Also note that some hypochromicity (absorption decrease) is noted for the polar solvent.

It is more difficult to determine if a frequency shift occurs with 2,4,6-TNT due to its broad and relatively flat peak maximum, but the data may suggest a hypsochromic shift (blue shift) of the $\pi \rightarrow \pi^{*}$ transitions, which can also be observed in polar solvents where the ground state is lowered relative to the excited state [43]. Due to the observed bathochromic and possible hypsochromic shifts of $\pi \rightarrow \pi^{*}$ electronic transitions of analytes in acetonitrile solutions, the wavelength for maximum Raman resonance enhancements may differ for the same HE materials in the solid phase. For this reason, previously observed resonance maxima by Conanescu et al. [32] may differ slightly (perhaps up to 10 nm) from solid samples. Additionally, the calculated values of Raman enhancements at particular wavelengths presented in this thesis may also differ slightly from actual values due to the same solvent effects shifting λ_{max} .

2.   Solid Explosive Raman Spectra

Raman spectra of select high explosive samples are shown in Figure 12 using a 785 nm excitation laser. Additional spectra can be found in Appendix A. Due to specific

vibrations that are influenced by the local chemical environment, each Raman spectrum is generally unique (i.e., a "fingerprint"). Military explosives are most commonly used in formulations with mixtures of other explosives and compounds to improve mechanical and chemical properties [32]. In Figure 12, the Raman spectral signature of Composition B, a mixture of TNT and RDX, is plotted along with pure samples of RDX and TNT. Although at first glance the Composition B Raman spectrum looks like that of TNT, a closer inspection reveals the presence of RDX peaks at ~890, ~1270, and ~1310 cm^{-1}. Composition B's Raman spectra also exhibits some broadband fluorescence which is likely due to the 1% paraffin wax it contains.
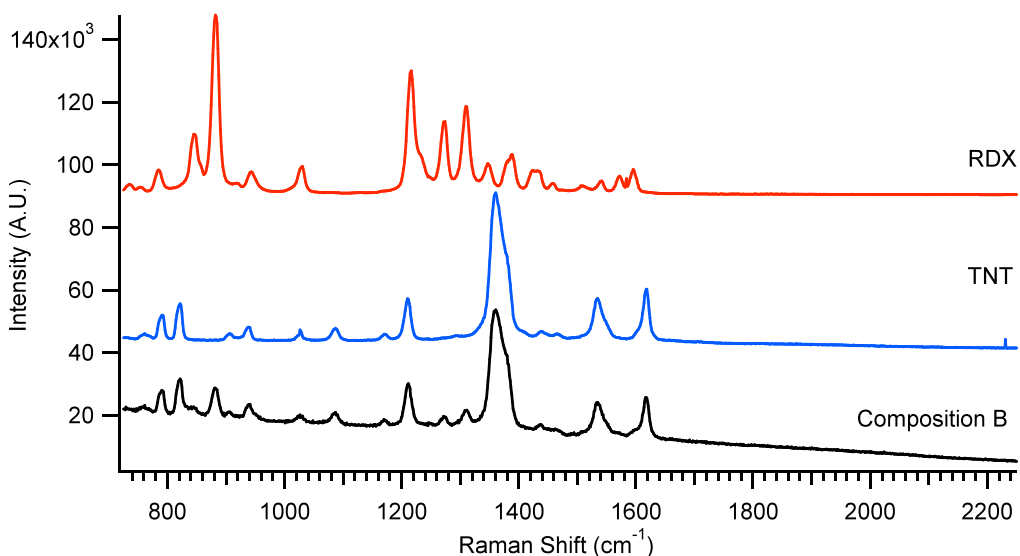
Figure 12.   Raman spectra of RDX, TNT and Composition B explosives acquired using a 785 nm laser at 50 mW. TNT and RDX are the principal explosive ingredients of Composition B, and their composite signatures are visible in the Composition B spectrum. TNT and RDX spectra are offset for clarity.

When Raman spectra are collected using an excitation wavelength at or near a strong electronic transition of the target molecule, the resulting spectrum is often different (even simplified) compared to a spectrum acquired with wavelengths far from strong transitions. The differences between these spectra are (in the absence of degradation) a result of resonance enhancement in which only the molecular vibrations associated with the electronic transition are amplified and appear in the acquired Raman spectrum. The other analyte peaks may be present but not visible if the enhancement is

46

strong. Since most molecules absorb in the ultraviolet spectral region, resonance Raman effects are often observed when using UV excitation wavelengths. For example, some Raman spectral simplification can be observed in the ultraviolet resonance Raman (UVRR) spectra of TNT and PETN compared to normal Raman as shown in Figures 13 and 14. This simplification can make qualitative determination easier in complicated sample matrices, but it can also make it more difficult when trying to distinguish between molecules with very similar molecular structures.

Figure 13.   Raman spectra of PETN using 785, 244, and 229 nm laser excitation wavelengths.
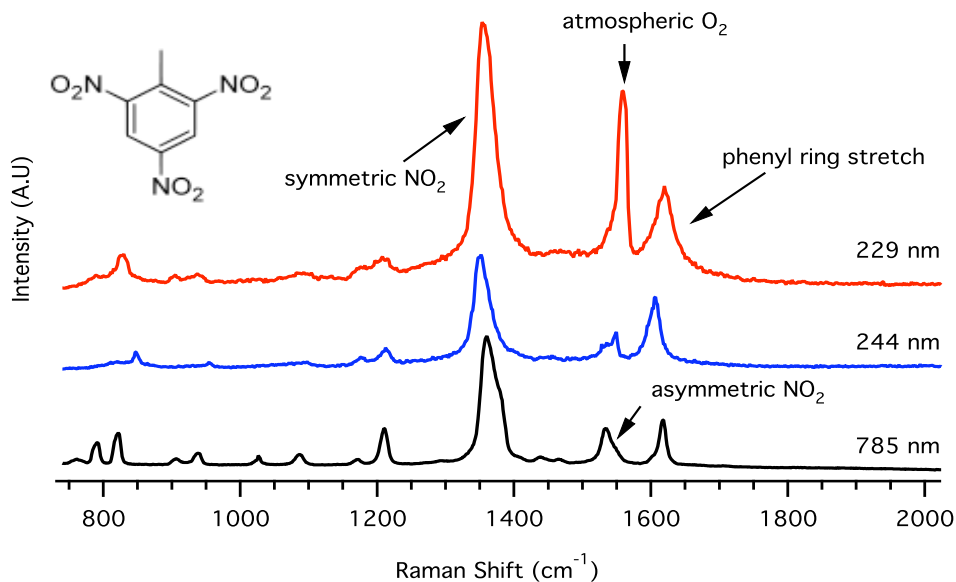
Figure 14.   Normalized Raman spectra of 2,4,6-TNT using a 785, 244, and 229 nm laser excitation wavelengths. The asymmetric NO_2 peak is clearly visible in the NIR Raman spectrum, but the atmospheric oxygen band ($\sim1585cm^{-1}$) in the 229 nm-excited spectrum fully obscures this analyte band.

The presence of the atmospheric O_2 Raman band in the UVRR spectrum is problematic for observing the asymmetric NO_2 stretch in most of the samples used in this study. For real-world standoff measurements, the O_2 band will most likely be the dominant Raman band in this spectral region and completely mask the weaker asymmetric NO_2 Raman band of the nitroaromatic explosives.

Figure 15 demonstrates that with sufficient detector resolution and signal to noise (S/N) it is possible to unambiguously identify analytes with very similar molecular structures using UVRR. 2,4-dinitrotoluene and 2,6-dinitrotoluene only differ by the location of one NO_2 group on the molecule's aromatic ring; still these spectra can be differentiated with sufficient S/N.
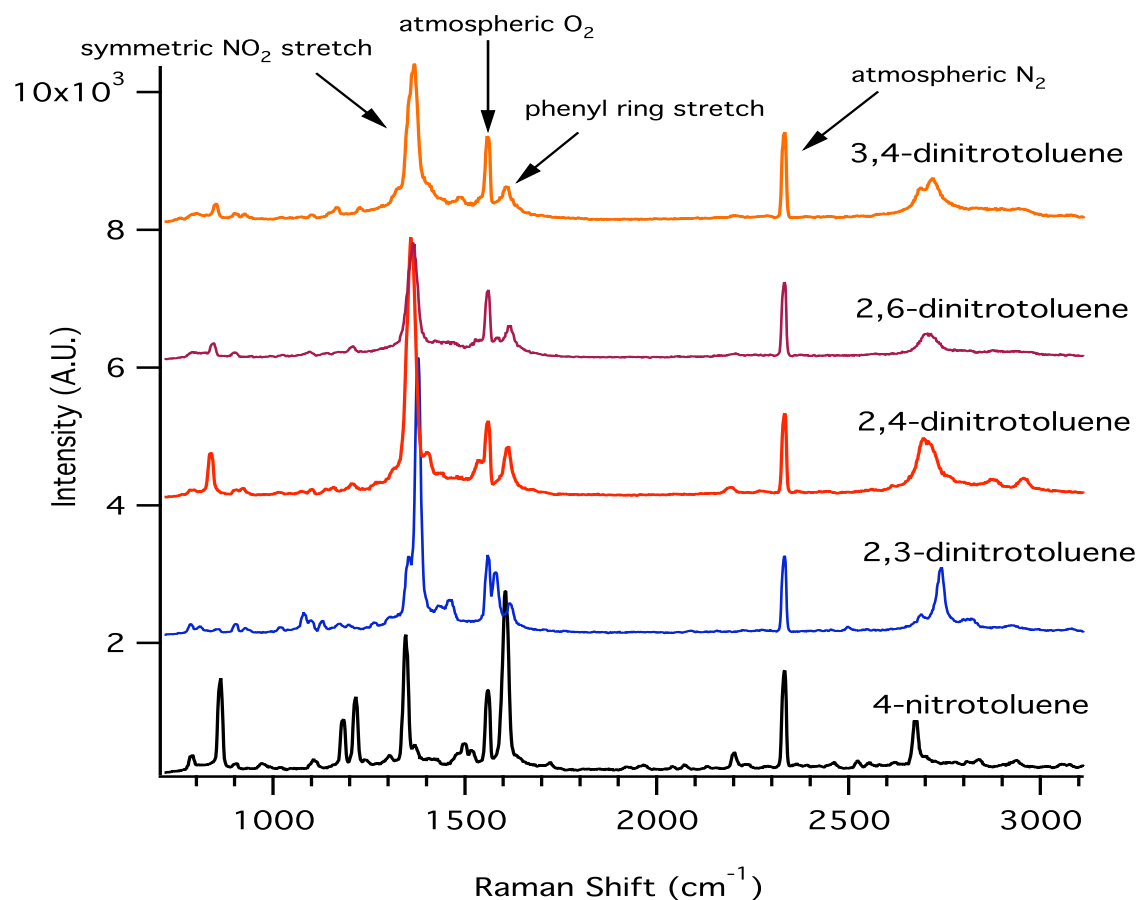
Figure 15.   Raman spectra of PNT; 2,3-DNT; 2,4-DNT; 2,6-DNT; and 3,4-DNT crystals collected using a 229 nm Raman microscope. Laser power was 0.27 mW with 180-second integration time for all spectra. Spectra are offset by 2000 counts for clarity. Sharp atmospheric O_2 and N_2 Raman lines are indicated.

Due to resonance effects, it is also possible to observe additional analyte vibrational bands in UVRR compared to normal Raman by amplification of bands that are otherwise very weak. This is a likely explanation for the appearance of additional peaks observed in ANFO's UVRR spectra shown in Figure 16. It is also common to observe overtones of other bands in UVRR spectra.
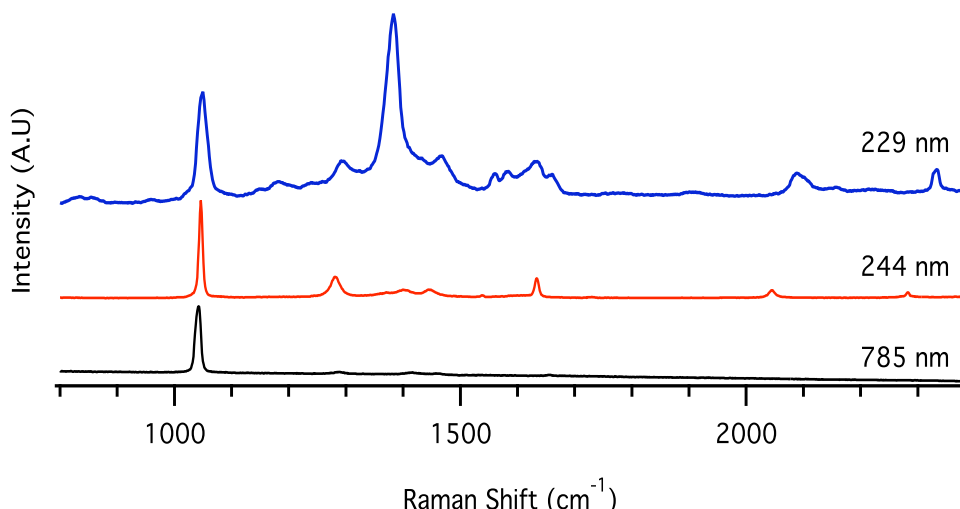
Figure 16.   Normalized Raman spectra of ANFO using 785, 244, and 229 nm laser excitation wavelengths. The Raman bands between 1200 to 1700 cm^{-1} are more pronounced at lower excitation wavelengths.

The acquisition of Raman spectra for RDX proved to be very challenging for UV excitation, even at low laser power settings while rastering the sample. The UVRR spectra of solid RDX, a molecule that is less stable than TNT, exhibits various broad band features that do not map well to any of the Raman spectral features in the NIR spectrum, as shown in Figure 17. The very poor results obtained for RDX in the UV may be a result of photodegradation of the molecule. Our UV results suggest that RDX would likely be difficult to detect in a sample matrix due to the rather ambiguous observable spectral features. However, RDX is most commonly used in formulations with other explosives (Comp B and C-4 are notable examples), so this drawback may not be a hindrance to tactical explosive detection efforts.
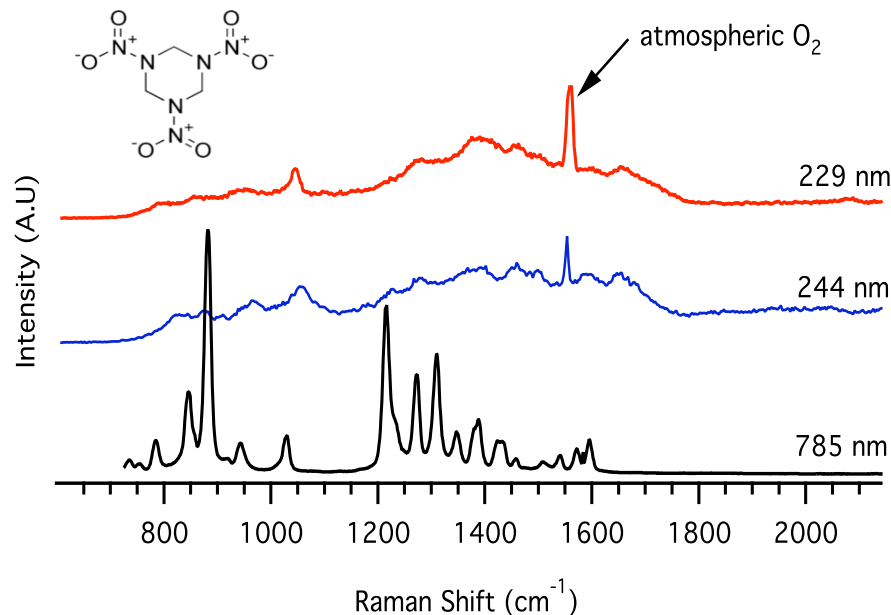
Figure 17.   Raman spectra of RDX using 785 nm, 244 nm, and 229 nm laser sources. The peak near 1550 cm^{-1} is atmospheric O$_2$.

3.   Raman Spectra of HE Solutions

Raman intensity measurements of the same sample while cycling through two laser power cycles from 0.025 to 2.2 mW were highly reproducible (<2% error). Raman measurements with the laser pointed (i.e., no rastering of the sample) at a fixed spot in PNT solution demonstrated an approximate 18% reduction in Raman intensity after five 180-second scans. This reduction in signal is likely due to index of refraction changes from localized sample heating and/or photodegradation. Rastering the laser across the solution samples produced highly reproducible Raman spectra for all samples and was the technique utilized for all quantitative measurements.

Since solute concentrations ranged from only 2.2 mM for UVRR analysis to 150 mM for NIR Raman analysis, the solvent (acetonitrile) Raman bands expectedly dominated the observed Raman spectra for sample solutions. Raman signatures of neat acetonitrile and PETN solution in acetonitrile are presented in Figure 18. The asymmetric and symmetric NO$_2$ peaks of PETN are clearly visible in the PETN solution spectrum.

51
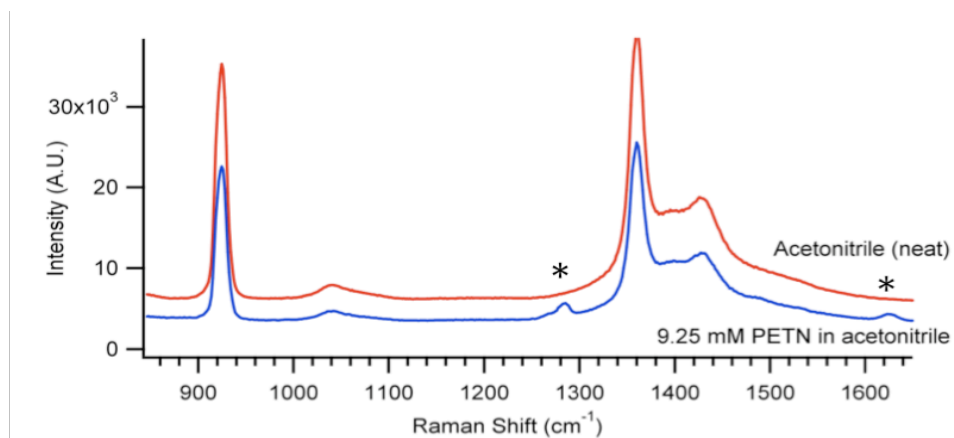
Figure 18.   Raman spectra of 9.25 mM PETN solution in acetonitrile (bottom) and neat acetonitrile (top) at 244 nm excitation. Laser power was 100 µW and the sample analysis time was 180 s. The 1282 cm^{-1} and 1650 cm^{-1} bands of PETN are small but visible and marked by an asterisk.

The UVRR spectra of TNT acquired at 244 and 229 nm excitation wavelengths are presented in Figures 19 & 20, respectively. The symmetric NO_2 stretch (~1340cm^{-1}) for the all of the aromatic compounds (i.e., PNT, DNT, TNT) studied were partially convolved with an acetonitrile peak.
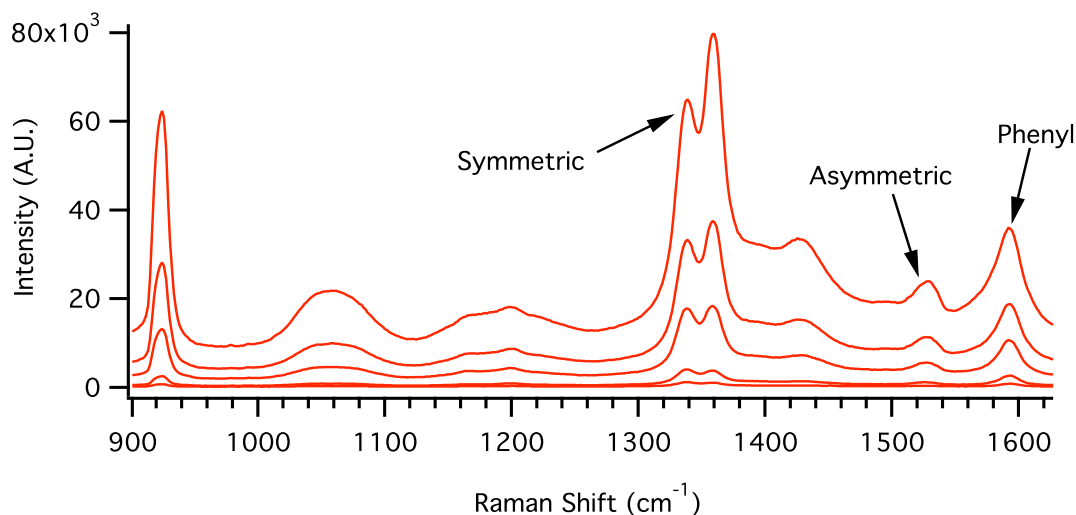
Figure 19.   Raman spectra of 2.2 mM 2,4,6-TNT in acetonitrile recorded at various laser power settings ranging from 25 µW (bottom) to 2.2 mW (top) using 244 nm laser excitation. Total accumulated CCD integration time for all spectra was 180 seconds to allow quantitative analysis of the integrated Raman band intensities. Symmetric and asymmetric NO_2 stretches and phenyl ring stretches of TNT are annotated.

52
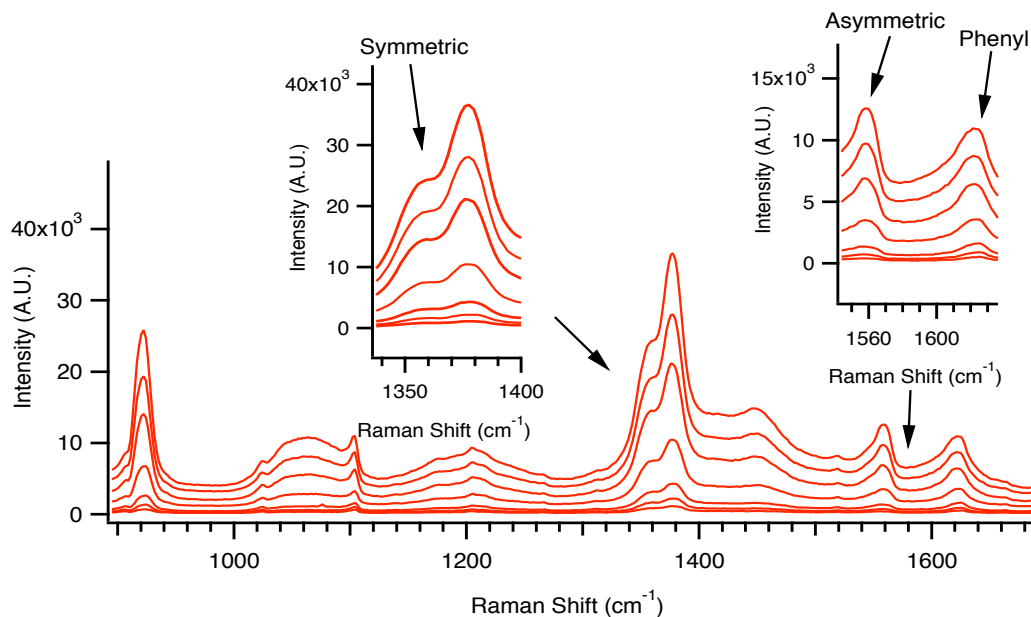
Figure 20.   Raman spectra of 2.2 mM 2,4,6-TNT in acetonitrile recorded at various laser power settings ranging from 25 μW to 0.95 mW using 229 nm laser excitation. The insets are an expanded view of the NO_2 and phenyl ring Raman modes regions. Total accumulated CCD integration time for all spectra was 180 seconds.

The integrated intensities for the TNT NO_2 and phenyl ring bands and the 919 cm^{-1} acetonitrile (internal standard) band were measured. The Raman intensities of the 919 cm^{-1} reference peaks were all linear with increasing power as predicted by Equation 3.1. The regression coefficient (R^2) was greater than 98%. The regression coefficients for PNT and 2,4-DNT analyte peaks were also highly linear. However, the regression coefficient of Raman band intensity versus power for the TNT NO_2 symmetric band is nonlinear with increasing laser power (see Figure 21).
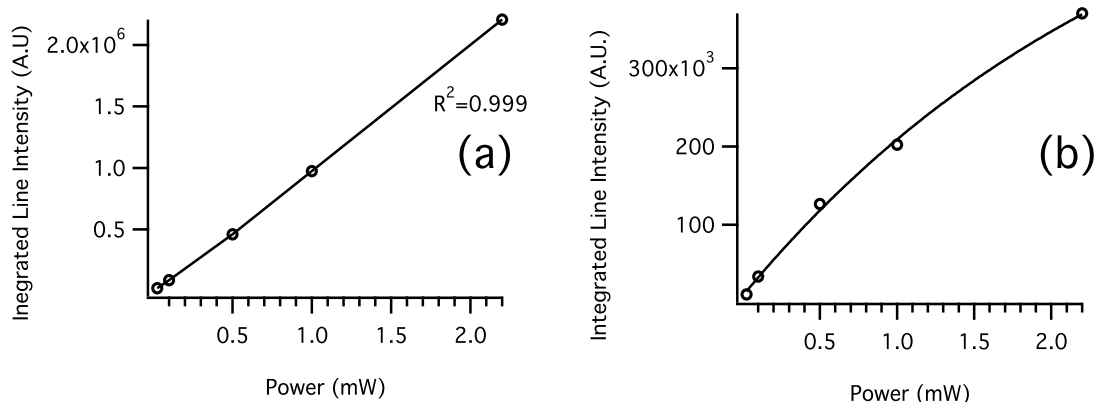
Figure 21.   (a) Integrated intensity of the 919 cm^{-1} acetonitrile reference band vs. laser power at 244 nm excitation. The result is highly linear as demonstrated by the regression coefficient indicated on the graph. (b) Integrated intensity of the 2,4,6-TNT symmetric NO$_2$ stretch vs. laser power for 244 nm excitation. This result is visibly nonlinear and can be fitted with an exponential function $(\text{constant} - \exp(-l))$.

The nonlinear results of integrated line intensities versus power can likely be attributed to photodegradation of the sample, but could theoretically be due to other nonlinear effects that will be discussed later.

B.   CALCULATED RAMAN ENHANCEMENT

The integrated Raman band intensity data combined with UV-Vis transmission data were used to calculate (refer to Equation 5.8) resonance Raman enhancements for various analyte bands in the Raman spectra acquired at 244 and 229 nm excitation (see Figures 22 to 25).   These reported Raman enhancements are solely due to resonance effects. It is important to note that the additional multiplicative enhancement gained from the well known frequency dependence (the integrated Raman scattering goes as ν^4) of the Raman scattered signal have been factored out in Equation 5.8 by ratioing to the acetonitrile reference bands.   The Raman enhancements for explosive analytes were generally found to decrease though a weak exponential function with increasing laser power. This is clearly demonstrated in Figure 22 with the phenyl ring stretch of TNT. This effect is most likely attributed to photodegradation, but could also arise from resonance dampening or saturation.   If photodegradation competes with the Raman

scattering process, the Raman scattering cross section will be reduced and enhancements will be decreased. Saturation effects are normally associated with high-pulsed power lasers and depletion of the ground state. A shift in the center frequency of the resonance curve at higher powers due to other nonlinear effects (such as nonlinear damping) is also possible but not likely in this case.

The uncertainty associated with the Raman resonance enhancement calculations using Equation 5.8 is estimated to be 16-18% based on propagation of experimental errors. The largest relative standard deviations are from Raman band area calculations and transmission measurements in the NIR region.

Figure 22.   Calculated Raman resonance enhancements for 2,4,6-TNT symmetric NO_2 stretch (left) and phenyl ring stretch (right) at 229 nm and 244 nm laser excitation using Equation 5.8.

For TNT, the most notable difference in resonance enhancements between the two UV wavelengths is with the Raman signal corresponding to the phenyl ring stretch. This stretch corresponds to an electronic transition centered at 260 nm in the UV-Vis spectra, so it is reasonable that enhancements at 244 nm are greater than those at 229 nm. The Resonance enhancements calculated for TNT's symmetric NO_2 stretch are indistinguishable due to experimental error.
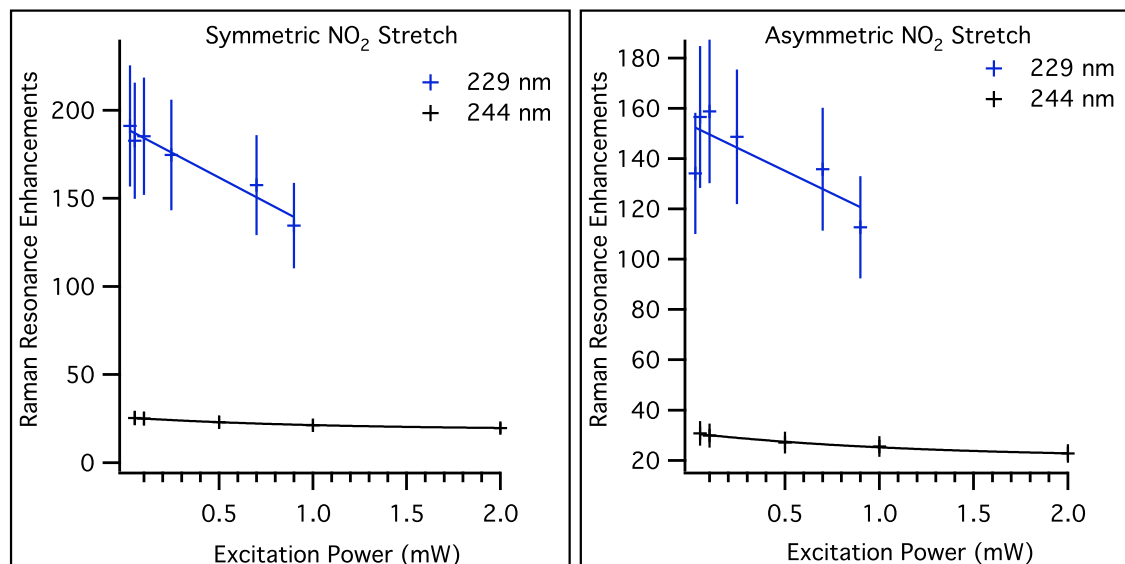
Figure 23.   Calculated Raman resonance enhancements for PETN symmetric NO_2 stretch (left) and asymmetric NO_2 stretch (right) at 229 nm and 244 nm.

For PETN it can be predicted from the UV-Vis spectrum in Figure 10 that there will be greater enhancements at 229 nm excitation compared to 244 nm for PETN, which was also observed experimentally for both the symmetric and asymmetric NO_2 stretch (see Figure 23).

The resonance enhancements for 2,4-DNT's phenyl ring stretch at 229 nm and 244 nm are generally indistinguishable owing to experimental error (see Figure 24). Based on the molar absorptivity of 2,4-DNT, it is predicted that 244 nm excitation will produce larger Raman resonance enhancements in the phenyl ring band than at 229 nm. The Raman enhancements for the NO_2 stretch were greater at 229 nm than at 244 nm.
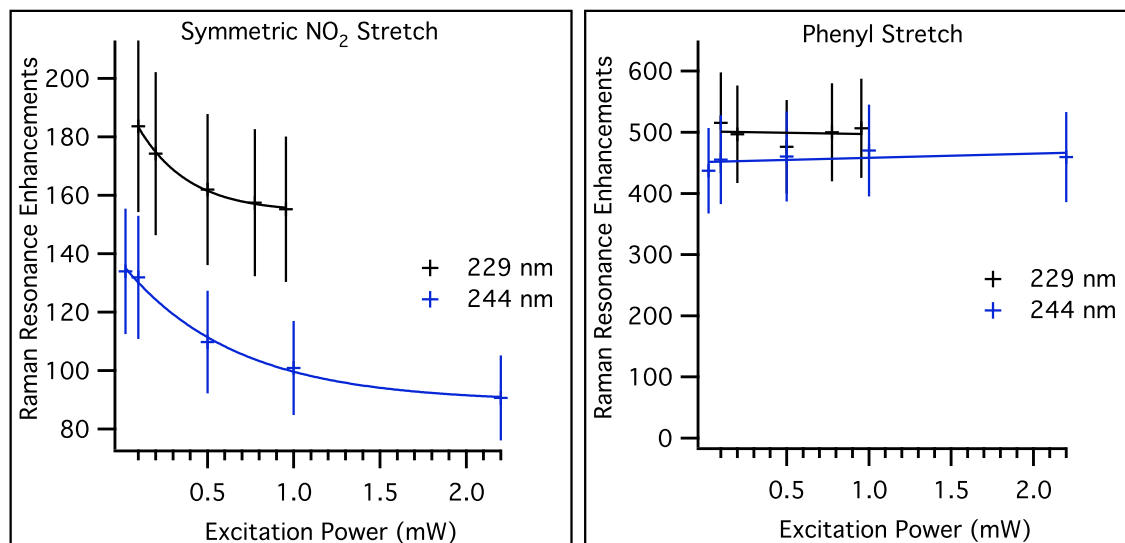
Figure 24.   Calculated Raman resonance enhancements for 2,4-DNT at 229 nm (left) and 244 nm (right).

The molar absorptivities on PNT at 229 nm and 244 nm are close in value since there is a minimum in the UV-Vis spectrum at 235 nm; however, excitation at 244 nm is closer to the $\pi \rightarrow \pi^{*}$ transition associated with the phenyl ring stretch. As a result, the observed Raman enhancements for the PNT phenyl stretch is more enhanced at 244 nm than 229 nm excitation.
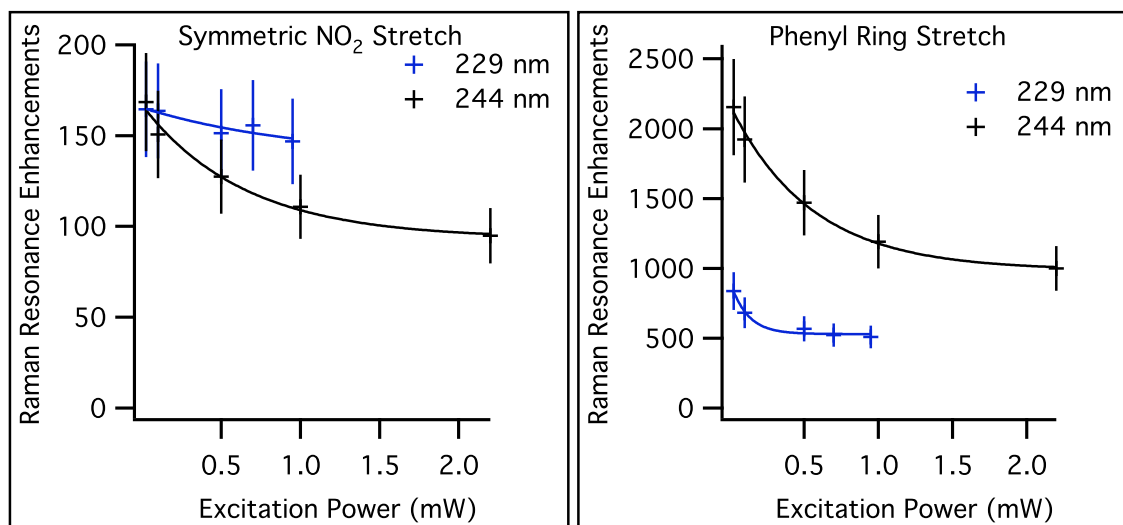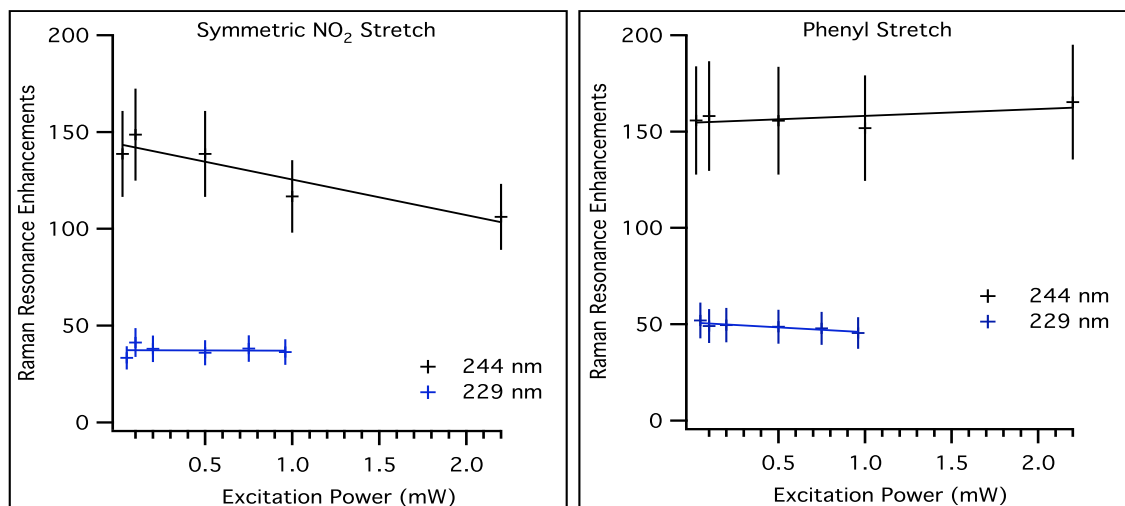

Figure 25.   Calculated Raman resonance enhancements of symmetric NO_2 stretch (left) and phenyl ring stretch (right) for PNT at 229 nm and 244 nm laser excitation.

Using the method presented in this thesis, it is also possible to qualitatively demonstrate the Raman resonance enhancement curves for 2,4,6-TNT as a function of wavelength by analyzing the data presented by Comanescu et al. [32]. The ratio of TNT Raman signal intensity to the acetonitrile (919 cm^{-1}) can be calculated directly from their presented data, but there is not enough information to accurately calculate quantitative resonance curves. Figure 26 demonstrates the relatively large bandwidth of the Raman resonance effect for TNT.
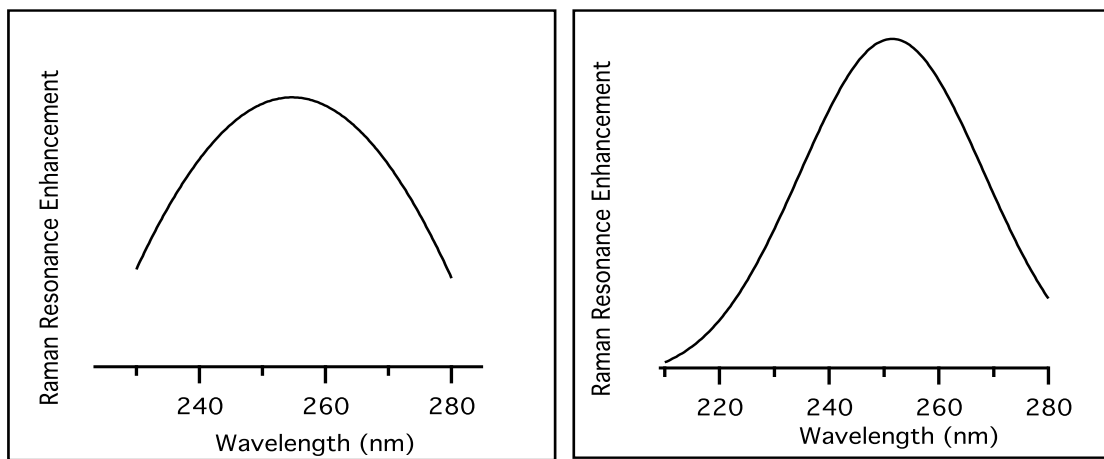
Figure 26.   Calculated Raman resonance enhancement curves for 2,4,6-TNT's symmetric NO$_2$ band (left) and phenyl ring stretch (right) using acetonitrile as an internal standard. Data from: [32]. Relative analyte / reference peak heights were fitted using a Gaussian curve. The wavelength of maximum Raman resonance effects for TNT's symmetric NO$_2$ stretch and phenyl ring stretch were reported to be 263 nm and 260 nm respectively [32].

C.   APPLICATION TO SOLIDS

There were several reasons why it was desirable to demonstrate a method to estimate Raman enhancements in solution and apply those results to solid phase samples. High explosives in solution are much easier to deal with than solid samples for safety reasons and many labs, including LLNL, have limitations on the quantities of explosives that can be used in certain facilities. Additionally, resonance enhancement studies require an internal standard reference, which is much easier to introduce in solution-based studies; internal standards can be dissolved in the solution or the solvent can serve

as the internal standard. For solids, the introduction of an internal standard is more difficult since heterogeneities in terms of particle sizes and distribution are present. This results in irreproducible measurements and large error especially when one considers that the typical laser beam spot size is on the order of tens of microns in diameter.

The effects of laser attenuation and self-absorption of the Raman signal were derived in the Methods section. The laser penetration depth and return Raman signal are functions of the optical (absorption and scattering coefficients) and physical (particle size and sample thickness) properties of the sample. The wavelength dependent laser penetration depths, evaluated using the integral inside Equation 5.14, are shown in figure 27 for 2,4,6-TNT and PETN. Since the wavelength of the Raman signal of the analyte varies with the excitation wavelength, the value of the molar absorptivity, ε_R, at each desired excitation wavelength must first be determined. Note: The biggest unknown material property, and the one most difficult to characterize, is the light scattering coefficient, which was not included in the model of Equation 5.14. It is recognized that future model improvements should include the scattering coefficient.
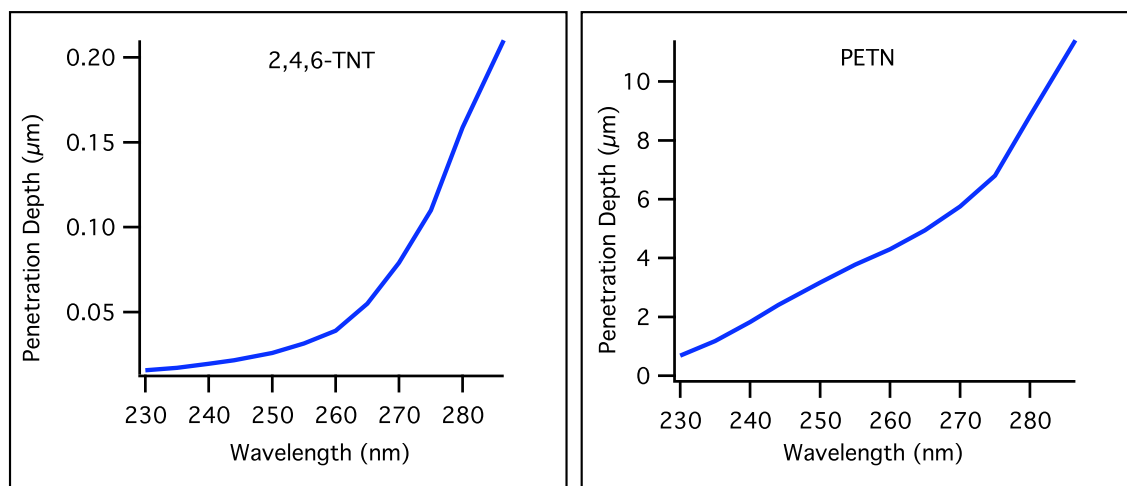
Figure 27.   Calculated penetration depth of the UV Raman signal for the phenyl ring stretch of 2,4,6-TNT (left) and symmetric NO_2 stretch of PETN (right).

From Figure 27, it is clear that the deep-UV excited Raman scattering from explosives will come from very near the sample surface. In general, UV excitation provides a higher Raman cross section for a sample, because of the dependence of the

Raman intensity on the inverse 4th power of the wavelength. However, for highly absorbing samples, or sample matrices, the exponential decrease of the penetration depth of the laser at UV wavelengths leads to an overall decrease of the measured signal. It may seem counterintuitive but in cases where resonance Raman enhancements are also realized, the optimal wavelength selection for maximizing the resonance enhancement may not necessarily be the optimal wavelength for achieving the highest Raman signal and sensitivity from the sample. As an example, NIR excitation has an obvious advantage over UVRR for non-absorbing bulk samples (i.e., thick samples) since this wavelength will penetrate deeper into the sample and provide more scattering that can be detected.

The resonance Raman enhancement calculation, using Equation 5.14, for the TNT phenyl ring stretch at 244 nm compared to 785 nm excitation is shown below. In Equation 7.1 all length dimensions are in cm, $\varepsilon_0(244nm) + \varepsilon_R(254nm)$ is 27500 $M^{-1}cm^{-1}$, c is 7.28 M, n (TNT solid) is ~1.64, n (TNT solution) is ~1.35:

$$
\begin{aligned}
E_S &\approx \frac{L_S}{L_{SOLN}} \left(\frac{\lambda_{NIR}}{\lambda_{UV}} \right)^4 E(\lambda)_{SOLN} \frac{\left[\int_0^D e^{-2.304bc(\varepsilon_0 + \varepsilon_R)} db \right]_{UV}}{\left[\int_0^D e^{-2.304bc(\varepsilon_0 + \varepsilon_R)} db \right]_{NIR}} \\
&= \frac{2 \cdot 10^{-6}}{D} \frac{L_S}{L_{SOLN}} \left(\frac{\lambda_{NIR}}{\lambda_{UV}} \right)^4 E(\lambda)_{SOLN} \\
&\approx \frac{5 \cdot 10^{-4}}{D} E(\lambda)_{SOLN}
\end{aligned}
\qquad (7.1)
$$

When Raman enhancements for TNT's phenyl stretch are of the order of microns (10^{-4} cm), the value of E_S is of the order of E_{SOLN}. For reference purposes, the deposits of explosive residues from fingerprints are typically less than 7 μm thick, which is thicker than the penetration depth of TNT at UV wavelengths [14].

The estimated total Raman enhancement, based on the model presented in equation 5.14, at UV wavelengths versus NIR wavelengths E_s for the TNT phenyl ring stretch, TNT symmetric NO_2 stretch, and PETN symmetric NO_2 stretch are presented in Table 3.

Raman Band	E_s / D (μm)
TNT Symmetric NO_2 (229 nm)	750
TNT Phenyl (229 nm)	2000
TNT Symmetric NO_2 (229 nm)	740
TNT Phenyl (229 nm)	6300
PETN Symmetric NO_2 (229 nm)	70000
PETN Symmetric NO_2 (244 nm)	11000

Table 3.   Total Raman enhancements (approximately ±25% error) compared to NIR Raman measurements, which factors in frequency enhancements and local field effects, are presented for TNT and PETN solids divided by the depth of the sample in microns. For TNT, the total enhancements for solids are of the same order of the resonance enhancements for solutions for micron size samples. For PETN, which has less laser absorption and Raman signal self-absorption, total enhancements are estimated to be greater than enhancements in solution.

It is important to recognize that this model has not been experimentally verified to date and the results from the calculations using equation 7.1 are only estimates. It was mentioned earlier that the current model does not include scattering coefficients for the solid. In addition, the refractive index values for TNT (solid) and acetonitrile are for measurements reported referenced to the Na line (589nm). Refractive index dispersion curves for TNT (solid) and acetonitrile are not available in the literature to our knowledge. For TNT, this may not be surprising since TNT has several polymorphs that would require measurements of each. In general, the refractive index of a material increases toward shorter wavelengths, which suggests that the refractive index values used in these calculations are on the low side.

Finally, the local field correction used in these calculations was described in the methods section. Briefly, the local field correction has mainly been applied in Raman spectroscopy when determining the absolute Raman cross section from liquid measurements [37, 38, 45, 47, 48, 49]. The local field correction is added to account for intermolecular interactions in the liquid (or solution) phase that are absent in the gas phase at low concentration. The local field correction in equation 7.1 is based on that used for calculating absolute Raman cross sections for gases using liquid measurements and, therefore, may not be the most appropriate correction for accounting for differences between solid and liquid phase intermolecular interactions.

VIII. CONCLUSION

A method was demonstrated to estimate pre-resonance and resonance enhancements of explosives and select explosive impurities in solutions using acetonitrile as an internal standard. Sample transmission and integrated Raman band intensities were calculated for sample solutions of PNT; 2,4-DNT; PETN; and 2,4,6-TNT. Spectral conditions between NIR Raman and UVRR systems were matched to the greatest degree possible; however, the use of the internal standard mitigates differences in spectral conditions to allow quantitative enhancement calculations. Enhancement measurements were corrected for concentration of the samples, sample transmission, quantum efficiencies of the detectors, and detector gain.

All molecules studied demonstrated appreciable pre-resonance enhancements ranging from a low of 20 for PETN's symmetric NO_2 stretch at 244 nm excitation to a high of 2200 for TNT's phenyl stretch at 244 nm. Additional multiplicative frequency enhancements result from UVRR measurements; this includes a 138-fold enhancement going from 785 nm to 229 nm excitation and 107-fold enhancement going from 785 nm to 244 nm. A model was presented to extend calculated Raman resonance enhancements in solution to total Raman enhancements for solid samples. Resonance enhancements are observed over a broad bandwidth; the interplay of the optical (i.e., absorption and scattering) and physical (e.g., particle size and thickness) properties of the sample and sample matrix, the magnitude of the resonance enhancement, and frequency enhancements must be explored to find the optimal excitation wavelength.

Observed polar solvent effects may slightly shift the wavelength where maximum resonance effects are observed and also alter the magnitude of the resonance enhancement at a given wavelength due to bathochromic and hypsochromic frequency shifts.

In addition to demonstrated Raman signal enhancements, the signal-to-noise ratio will also likely be improved in UVRR measurements from the reduction of fluorescence interference and other interference due to operation in the UV solar blind region. Final

quantitative assessment of the UVRR standoff Raman signal strengths should also incorporate atmospheric attenuation, especially from ozone, and reflection losses from the sample surface.

Since different HE molecules have different excitation wavelengths where the Raman signals are at a maximum intensity, it may be desirable to use a tunable source for explosive detection if the required analysis time and spectrometer performance allows. Several detection schemas are possible. A UV wavelength could be chosen to give the greatest resonance effects to a number of prioritized analytes. For example, if TNT, PETN and RDX form the most proliferated explosive threats, the compounds and their Raman signal strength at a given wavelength could be weighted to select the best performance of the system. It may also be desirable to select two wavelengths that optimize performance for the greatest number of analytes. Another interesting concept is to combine UV and NIR or visible measurements to specifically look for resonance enhancements in HE samples to help prevent false positive alarms.

The overriding goal and motivation of this research was to demonstrate possible enhancements that extend to the standoff detection of explosives. UVRR spectroscopy appears to be more promising in detecting explosive residues than NIR measurements due to resonance enhancements, improved scattering efficiency due to frequency enhancements, and the reduction in background noise.

IX.   RECOMMENDATIONS

In order to continue to progress in standoff explosive detection, it is recommended that a variety of additional experiments be performed. This research will provide additional insight into the military feasibility of Raman spectroscopy in the standoff detection of explosives.

A.   HIGH EXPLOSIVE SAMPLES

TNT, DNT, & PNT were interesting molecules to study to learn more about the most important factors that contribute to resonance effects in Raman of high explosives. TNT displays stronger resonance enhancements than DNT and PNT. This may be due to the combination of increased molecular symmetry and higher molar absorptivity at the selected wavelengths of study. The future study of 1,3,5-trinitrobenze, an explosive molecule with a high level of symmetry, may help elucidate the factors that are most important to resonance Raman.

Other HE molecules and formulations should also be studied including TATP, Composition B, ANFO, C4, Semtex, and nitromethane.

B.   EQUIPMENT DISCUSSION

The Swept-Wavelength Optical resonance-Raman Device (SWORrD) system used in the previous NRL study allowed for the rapid qualitative analysis of Raman resonance effects from 210 to 280 nm. A similar tunable system with a $180°$ collection geometry for solid and solution samples would be ideal to rapidly explore Raman resonance quantitatively using the method described in this thesis.

C.   MODEL VERIFICATION

The model presented in Equation 5.14 for estimating the resonance Raman of solids using solution data requires experimental verification. In all likelihood this will require basic measurements of some of the unreported optical and physical properties of the HE materials.

D. STANDOFF DETECTION

Standoff UVRR measurements using LLNL's pulsed alexandrite laser system are scheduled to begin in the near future under laboratory conditions. The use of a spun sample matrix with a solid internal standard should be explored to quantify Raman resonance effects at standoff distances. Spinning the sample should help mitigate heterogeneity in the sample which can skew results.

If laboratory standoff UV Raman measurements are favorable, field standoff UVRR measurements of a wide variety of target sets would be the next step.

APPENDIX A.   ADDITIONAL SPECTRA

A.   785 NM SPECTRA

1.   Standards

See reference [17] for shift standard peak locations of the Raman shift standards.
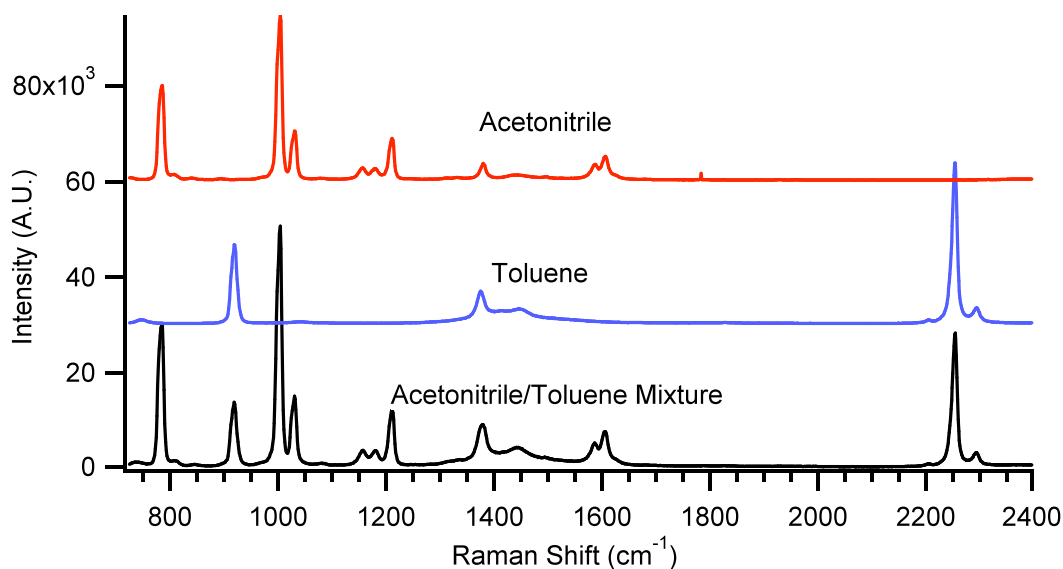
Figure 28.   The spectra of acetonitrile, toluene, and a 50% v/v mixture of toluene/acetonitrile using a 785 nm laser are presented.
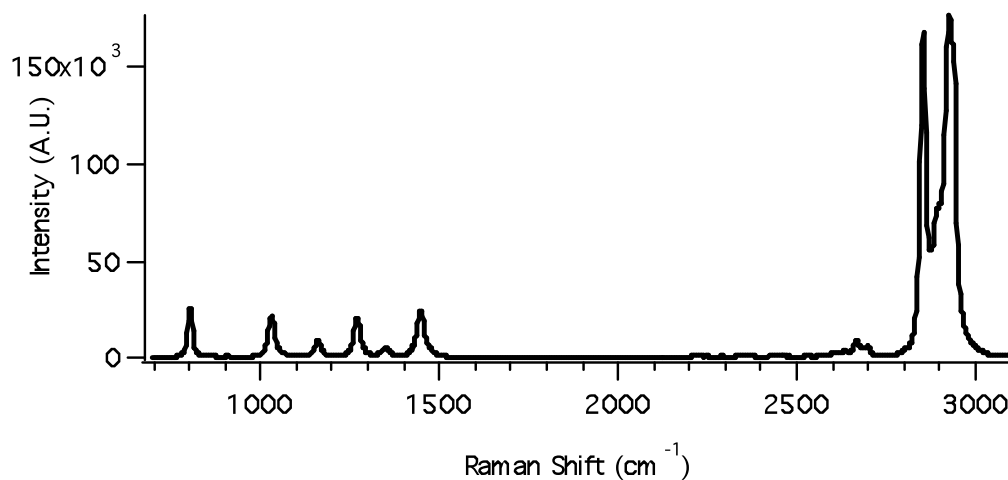
Figure 29.   Raman spectra of cyclohexane used to calibrate the UVRR system at 229 nm. Acetonitrile/toluene is not suitable due to the absorption edge in the deep UV.

2. Explosives

The following HE Raman spectra are presented, but were not included in the main body of this thesis.
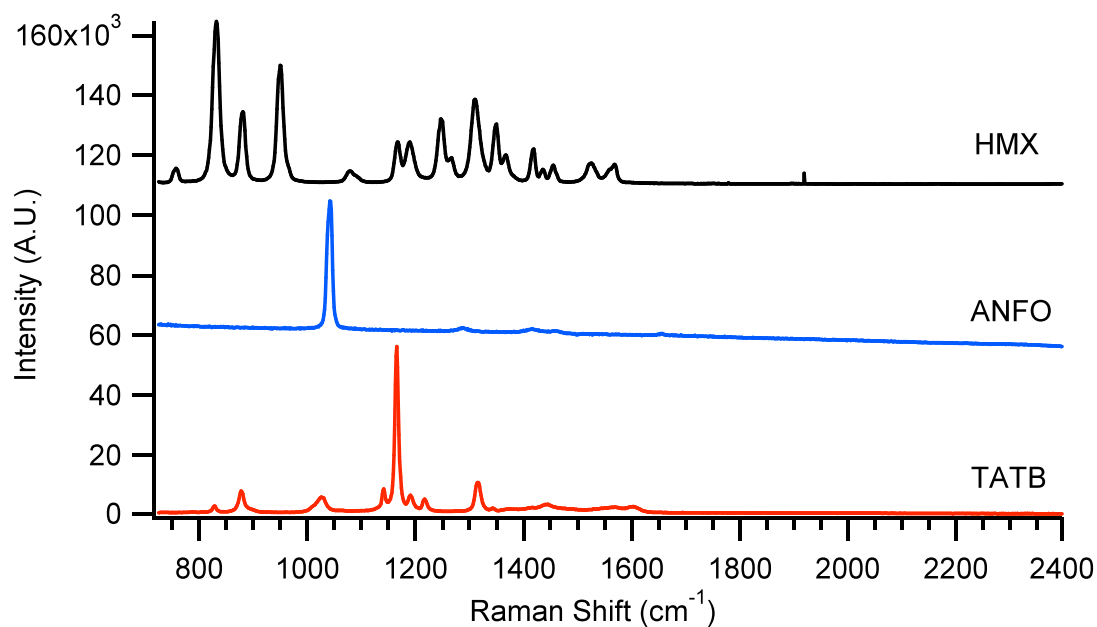
Figure 30.   Raman spectra of HMX, ANFO and TATB crystals collected using a 785 nm excitation Raman spectrophotometer. ANFO and HMX spectra are offset for clarity.
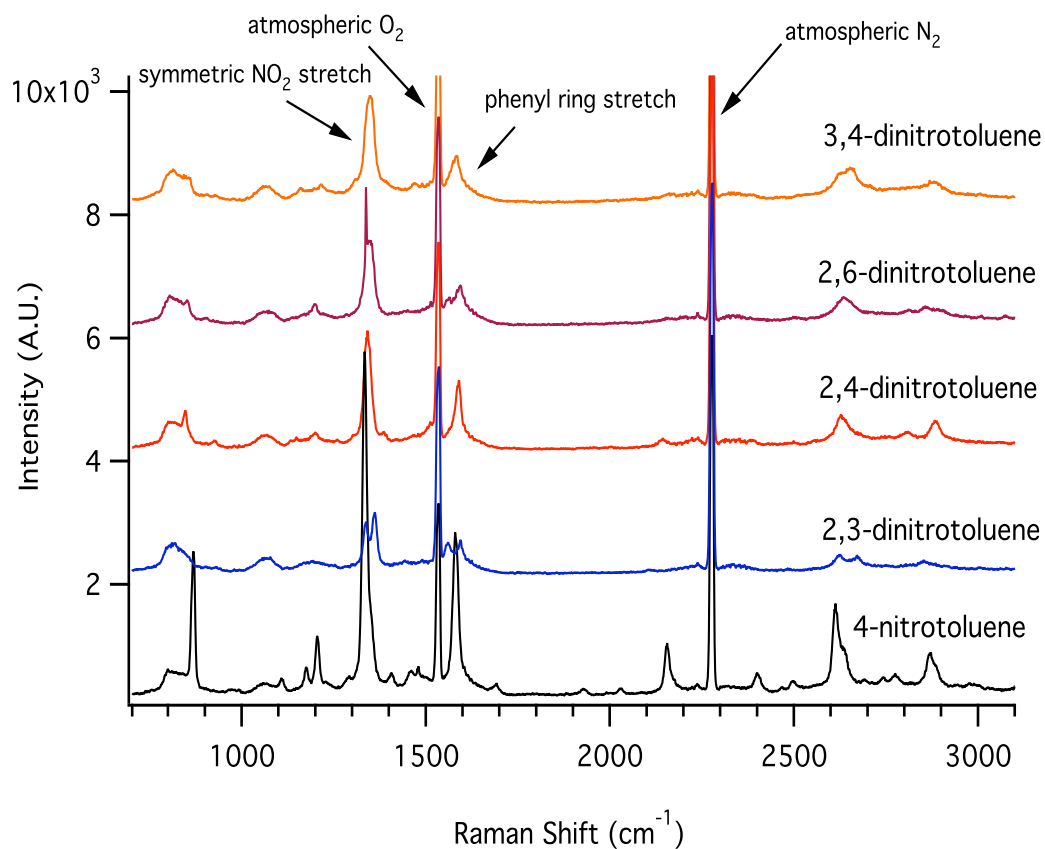
Figure 31.   Raman spectra of 3,4-DNT; 2,4-DNT; 2,6-DNT; 2,3-DNT; and PNT crystals collected using a 244 nm Raman microscope. Laser power was 2.1 mW with 180- second integration time for all spectra. Spectra are shifted up 2000 counts for clarity. Sharp atmospheric O_2 and N_2 Raman lines are visible as indicated.
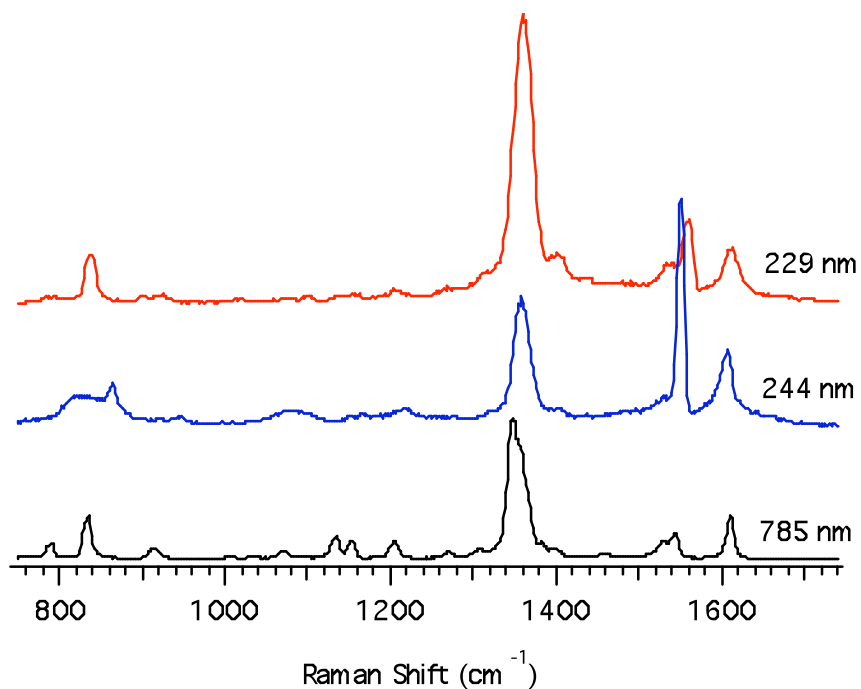
Figure 32.   Normalized Raman spectra of 2,4-DNT crystals collected using at 785 nm (50 mW), 244 nm (2.2 mW), and 229 nm (0.27 mW) 180 seconds. The symmetric NO_2 stretch is the much more intense than the asymmetric NO_2 stretch band, as would be expected based on Raman selection rules. The phenyl ring stretch, which is very symmetric in nature, is also a strong band. The atmospheric O_2 band convolves the NO_2 asymmetric stretch.
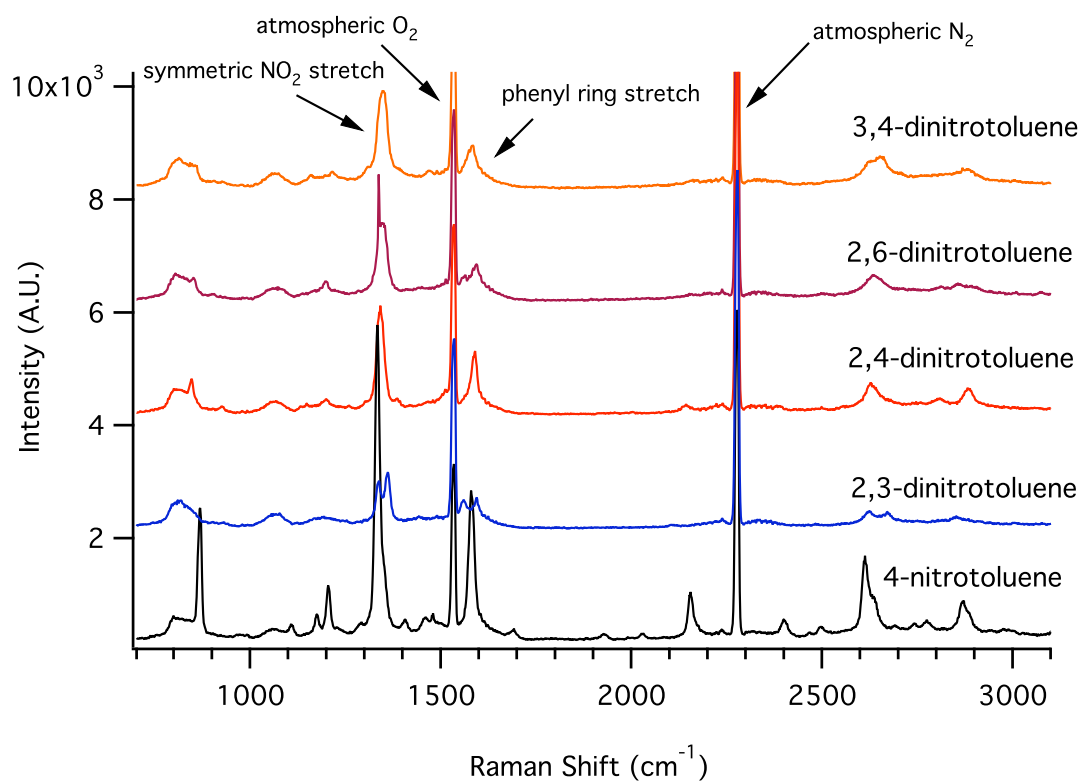
Figure 33.　　Raman spectra of 3,4-DNT; 2,4-DNT; 2,6-DNT; 2,3-DNT; and PNT crystals collected using a 244 nm Raman microscope. Laser power was 2.1 mW with 180 second integration time for all spectra. Spectra are offset by 2000 counts for clarity. Sharp atmospheric O_2 and N_2 Raman lines are visible as indicated.
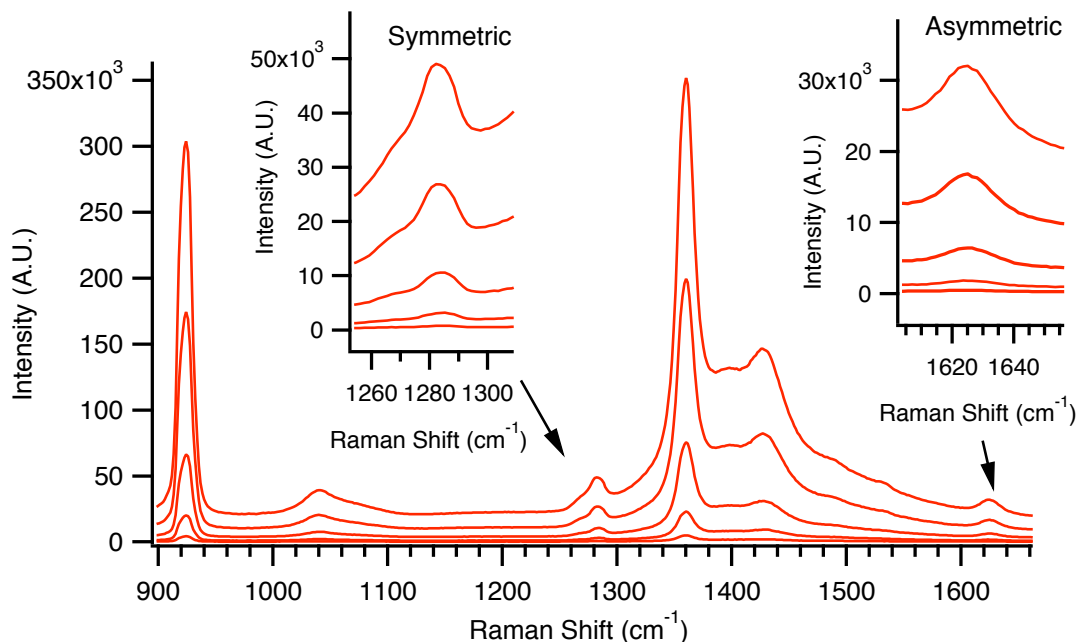
Figure 34.   Raman spectra of 9.25 mM PETN in acetonitrile recorded at various laser power settings ranging from 20 µW to 2.2 mW using a 244 nm laser excitation. Total accumulated CCD integration time for all spectra was 180 seconds to allow quantitative analysis of the integrated band intensities to be performed. The symmetric NO_2 (1282 cm^{-1}) and (1625 cm^{-1}) and asymmetric NO_2 stretches are expanded.
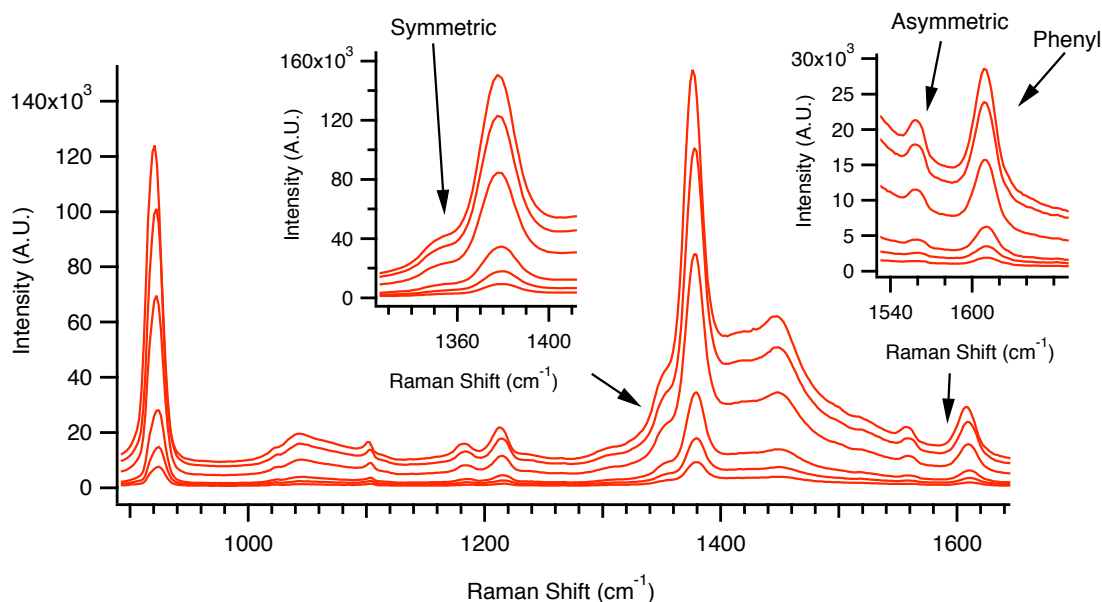
Figure 35.   Raman spectra of 3.43 mM PNT in acetonitrile recorded at various laser power settings ranging from 25 µW to 0.95 mW using 229 nm laser excitation. Total accumulated CCD integration time for all spectra was 180 seconds.

72
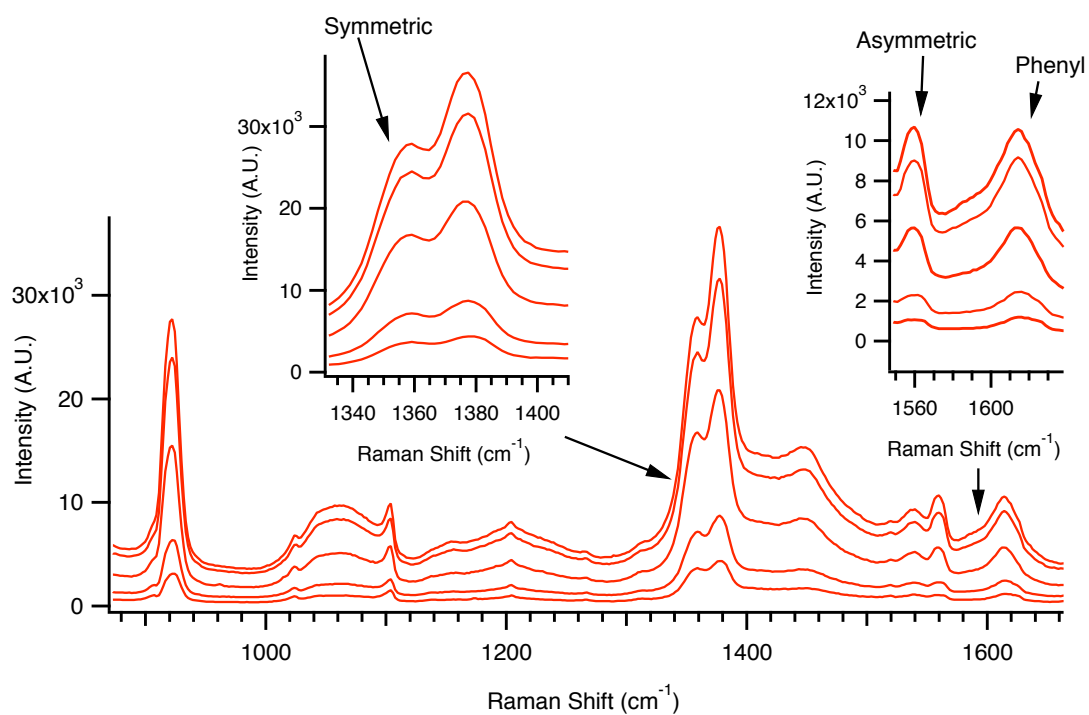
Figure 36.   Raman spectra of 2.43 mM 2,4-DNT in acetonitrile recorded at various laser power settings ranging from 25 μW to 0.95 mW using 229 nm laser excitation. Total accumulated CCD integration time for all spectra was 180 seconds.

THIS PAGE INTENTIONALLY LEFT BLANK

APPENDIX B. MATLAB CODE

This source code is provided without any warranties on performance. The user is advised to test the source code thoroughly before relying on it. The user must assume the entire risk of using the source code.

A. PEAK AREA ALCULATIONS

```
% peak_area_v3
% Created by Christine Paulson, Chance Carter & modified by Maj Bill
% Short
% Last modified 03/23/2009
% Lawrence Livermore National Laboratory

% This is a MATLAB m-file designed to read a spectra, user select two
% points for a baseline, compute a baseline, and then integrate the
% area between the two points.

close all; clear all;
cd('C:\Documents and Settings\') % input correct user directory
% USER SELECTS A FILE
[FileName,PathName] = uigetfile('*.txt','Select the spectra file.');

% LOAD FILE AND CUMULATIVE SUM
S2 = load([PathName FileName]);

% Data format: this program will be looking for data in two columns
% separated by tabs.
% The x column is comprised of Raman shift data with the y column
% containing count intensity.

S1 = S2(:,2)'; % select the y column and change the data format to a
% single row.

S1 = cumsum(S1,1); %cumulative sum, in case of multiple frames

% MAKE PLOT
figure; plot(S1, 'k', 'LineWidth', 1); title(FileName); axis tight;
hold on;

% USER SELECTS PEAK BOUNDARIES
datacursormode on
disp('SELECT THE PEAK BOUNDARIES ON THE FIGURE');
disp('HOLD DOWN THE "alt" KEY TO SELECT THE SECOND POINT');
```

```matlab
quit = 'n';
while(quit ~= 'y')

    disp(''); disp('')
    input('Press any key when peak selected.', 's')
    dcm_obj = datacursormode(gcf);
    info = getCursorInfo(dcm_obj);
    pos = [info.DataIndex];
    xval = [info.Position];
    xval = xval(1:2:end);
    disp(['You selected positions:  '])
    disp(xval)

    % COMPUTE BASELINE
      baseline_type = 3;
      xval = sort(xval);
      peakwidth = xval(2) - xval(1);
      if baseline_type == 1 %'midpoint'
            baseline = ones(peakwidth,1).* (S1(xval(1)) +
S1(xval(2)))/2;
      elseif baseline_type == 2 % 'halfpeak'
            baseline = ones(peakwidth,1).* min([ S1(xval(1))
S1(xval(2))]);
      else  %baseline linear fit
            increment = (S1(xval(2))-S1(xval(1)))/peakwidth;
            baseline = S1(xval(1)):increment:S1(xval(2));
    end
    plot(xval(1):xval(2), baseline, 'r', 'LineWidth', 1.5);
    plot(xval(1):xval(2), S1(xval(1):xval(2)), 'r', 'LineWidth', 1.5);

    %COMPUTE AREA
      S1_subtract = S1(xval(1):xval(2)) - baseline;
      area = sum(S1_subtract);

    disp(area)

    % Create textbox

    annotation(gcf,'textbox','String',{['Peak Area = '
num2str(area)]},'FontSize',16,...
        'FontName','Arial',...
        'FitHeightToText','off',...
        'LineStyle','none',...
        'Position',[0.1533 0.7667 0.3288 0.1284]);

    quit = input('Do you want to quit?  (y/n):  ', 's');
end
```

B. PEAK AREA CALCULATIONS BASED ON HALF OF AN OBSERVABLE CONVOLVED PEAK

```
% peak_area_v3
% Created by Christine Paulson & modified by Maj Bill Short
% Last modified 03/23/2009
% Lawrence Livermore National Laboratory

% This is a MATLAB m-file designed to read a spectra, user select two
% points for a baseline, compute a baseline, and then integrate a peak
% area of a partially convolved peak by exploiting peak symmetry.
% User will select the beginning of the peak and peak maximum.  Then
% user selects 'L' or 'R' to tell the
% program to compute the full the area from left to right or right to
% left, based on which portion of the peak is observable.

%USER SELECTS A FILE
[FileName,PathName] = uigetfile('*.txt','Select the spectra file.');

% LOAD FILE AND CUMULATIVE SUM
D = load([PathName FileName]);

%March 20, 2009 - inserted data format change
S1 = D(:,2);

figure;
plot(D(:,2))

% USER SELECTS PEAK BOUNDARIES
datacursormode on
disp('SELECT THE BASELINE POINTS');
disp('HOLD DOWN THE "alt" KEY TO SELECT THE SECOND POINT');
quit = 'n';
while(quit ~= 'y')

    disp(''); disp('')
    input('Press any key when peak selected.', 's')
    dcm_obj = datacursormode(gcf);
    info = getCursorInfo(dcm_obj);
    pos = [info.DataIndex];
    xval = [info.Position];
    xval = xval(1:2:end);
    disp(['You selected positions:  '])
    disp(xval)

    % COMPUTE BASELINE
    baseline_type = 3;
```

```matlab
    xval = sort(xval);
    peakwidth = xval(2) - xval(1);
    if baseline_type == 1 %'midpoint'
        baseline = ones(peakwidth,1).* (S1(xval(1)) + S1(xval(2)))/2;
    elseif baseline_type == 2 % 'halfpeak'
        baseline = ones(peakwidth,1).* min([ S1(xval(1))
S1(xval(2))]);
    else  %baseline linear fit
        increment = (S1(xval(2))-S1(xval(1)))/peakwidth;
        baseline = (S1(xval(1)):increment:S1(xval(2)));
    end

    cropS1 = S1(xval(1):xval(2));
    figure;
    plot(xval(1):xval(2), baseline, 'r', 'LineWidth', 1.5); hold on;
    plot(S1);
    plot(xval(1):xval(2), cropS1, 'r', 'LineWidth', 1.5);

    figure;
    S1_subtract = cropS1' - baseline;
    plot(xval(1):xval(2), S1_subtract, 'g')
    disp('SELECT THE PEAK POINT');
    disp(''); disp('')
    input('Press any key when peak selected.', 's')
    dcm_obj = datacursormode(gcf);
    info = getCursorInfo(dcm_obj);
    pos2 = [info.DataIndex];
    xval2 = [info.Position];
    xval2 = xval2(1:2:end);
    disp(['You selected position:  '])
    disp(xval)

leftorright = input('Enter "R" for right or "L" for left:   ', 's');
    disp(''); disp('')
    if leftorright == 'R'
        x2 = xval2:xval(2); x2 = x2 - xval(1)+1;
        S1_R = S1_subtract(x2);
        area_half = sum(S1_R)
    else
        x2 = xval(1):xval2; x2 = x2 - xval(1) + 1;
         S1_L = S1_subtract(x2);
                area_half = sum(S1_L)
    end

        quit = input('Do you want to quit?  (y/n):  ', 's');
end
```

LIST OF REFERENCES

[1]   National Research Council (U.S.), *Existing and Potential Standoff Explosives Detection Techniques.* Washington, D.C.: National Academies Press, 2004.

[2]   J. A. Zukas and W. P. Walters, Ed., *Explosive Effects and Applications. High Pressure Shock Compression of Condensed Matter*, New York: Springer, 2003.

[3]   P. E. Eaton, M. X. Zhang, R. Gilardi, N. Gelber, S. Iyer, and R. Surapaneni, "Octanitrocubane: a new nitrocarbon," *Propellants and Explosive Pyrotechnics*, vol. 27, no. 1, pp. 1-6, 2002.

[4]   J. Oxley, J. Smith, J. Brady, F. Dubnikova, R. Kosloff, and L. Zeiri, L, "Raman and infrared fingerprint spectroscopy of peroxide-based explosives," *Applied Spectroscopy*, vol . 62, no. 8, pp. 906-915, Aug. 2008.

[5]   J. D. Ingle and S. R. Crouch, *Spectrochemical Analysis*. Englewood Cliffs, N.J.: Prentice Hall, 1988.

[6]   D. S. Moore, "Instrumentation for trace detection of high explosives." *Review of Scientific Instruments*, vol. 75, no. 8, p. 2499, Aug. 2004.

[7]   C. L. Rhykerd, *Guide for the selection of commercial explosives detection systems for law enforcement applications*. NIJ guide 100-99, Washington, DC: U.S. Dept. of Justice, Office of Justice Programs, National Institute of Justice, 1999.

[8]   M. Fisher, *Explosive Chemical Signature-Based Detection of IEDs*. Ft. Belvoir: Defense Technical Information Center. http://handle.dtic.mil/100.2/ADA430111.

[9]   C. N. Sheaff, D. Eastwood, C. M. Wai, and R. S. Addleman, "Fluorescence Detection and Identification of Tagging Agents and Impurities Found in Explosives, *Applied Spectroscopy,* vol. 62, no. 7, p. 739, Jul. 2008.

[10]   P. C. Womble, G. Vourvopoulos, J. Paschal, I. Novikov, and G. Chen, "Optimizing the signal-to-noise ratio for the PELAN system," *Nuclear Instruments and Methods in Physics Research Section* A, vol. 505, pp. 470-473, 2003.

[11]   J. B. Miller and G. A. Barrall, "Explosives detection with nuclear quadrupole resonance - an emerging technology will help to uncover land mines and terrorist bombs," *American Scientist*, vol. 93, p. 50, 2005.

[12]   R. L. Woodfin, *Trace Chemical Sensing of Explosives*. Hoboken, N.J.: Wiley, 2007.

[13]   M. Prather, *Field Collection and Analysis of Forensic and Biometric Evidence Associated with IEDs*. Ft. Belvoir: Defense Technical Information Center, 2005. http://handle.dtic.mil/100.2/ADA433085.

[14]   R. R. Kunz, J. D. Hybl, J. D. Pitts, M. Switkes, R. Herzig-Marx, F. L. Leibowitz, L. Williams, and D. R. Worsnop, *Measurement of Explosive Residues Associated with Assembly and Deployment of IEDs*. Report No. 81-1004, Lexington, MA: Massachusetts Institute of Technology Lincoln Laboratory, 2006.

[15]   M. Swartz and I. S. Krull, *Analytical Method Development and Validation*. New York: M. Dekker, 1997.

[16]   C. V. Raman, *The molecular scattering of light*. Nobel Lecture, December 11, 1930.

[17]   R. L. McCreery, *Raman Spectroscopy for Chemical Analysis*. Chemical Analysis, Vol. 157, New York: John Wiley & Sons, 2000.

[18]   E. Smith and G. Dent, *Modern Raman Spectroscopy: a Practical Approach*. Hoboken, NJ: J. Wiley, 2005.

[19]   J. C. Carter, S. M. Angel, M. Lawrence-Snyder, J. Scaffidi, R. E. Whipple, and J. G. Reynolds, "Standoff detection of high explosive materials at 50 meters in ambient light conditions using a small raman instrument," *Applied Spectroscopy*, vol. 59, no. 6, pp. 769-775, Jun. 2005.

[20]   S. A. Asher, "UV resonance raman studies of molecular structure and dynamics: applications in physical and biophysical chemistry," *Annual Review of Physical Chemistry*, vol. 39, pp. 537-88, 1988.

[21]   M. J. Pelletier, *Analytical Applications of Raman Spectroscopy*. Osney Mead, Oxford: Blackwell Science, 1999.

[22]   J. A. Koningstein, *Introduction to the Theory of the Raman Effect*. Dordrecht: Reidel, 1972.

[23]   M. Fryling, C. J. Frank, and R. L. McCreery, "Intensity Calibration and Sensitivity Comparisons for CCD/Raman Spectrometers," *Applied Spectroscopy*, vol. 47, no. 12, p. 1965, Dec. 1993.

[24]   D. A. Skoog and J. J. Leary, *Principles of Instrumental Analysis*. Fort Worth: Saunders College Pub, 1992.

[25]   Z. Iqbal, K. Suryanarayanan, S. Bulusu, and J. R. Autera, *Infrared and Raman*

Spectra of 1,3,5-trinitro-1,3,5-triaziacyclohexane (RDX). Picatinny Arsenal: Defense Technical Information Center, 1972. http://handle.dtic.mil/100.2/AD752899.

[26]   Z. Iqbal, S. Bulusu, and J. R. Autera, "Vibrational spectra of beta-cyclotetramethylene tetranitramine and some of its isotopic isomers," *Journal of Chemical Physics*, vol. 60, p. 221, 1974.

[27]   I. P. Hayward, T. E. Kirkbride, D. N. Batchelder, and R. J. Lacey, "Use of a Fiber Optic Probe for the Detection and Identification of Explosive Materials by Raman Spectroscopy," *Journal of Forensic Sciences*, vol. 40, no. 5, p. 883, 1995.

[28]   C. Cheng, T. E. Kirkbride, D. N. Batchelder, and R. J. Lacey, "In Situ Detection and Identification of Trace Explosives by Raman Microscopy," *Journal of Forensic Sciences*, vol. 40, no. 1, p. 31, 1995.

[29]   Lewis, I. R., Daniel, N. W., Chaffin, N. C., Griffiths, P. R., & Tungol, N. W., "Raman spectroscopic studies of explosive materials: towards a fieldable explosives detector," *Spectrochimica Acta Part A.*, vol. 51, no. 12, pp. 1985-2000, 1995.

[30]   H. S. Sands, I. P. Hayward, T. E. Kirkbride, R. Bennett, R. J. Lacey, and D. N. Batchelder, "UV-excited resonance raman spectroscopy of narcotics and explosives," *Journal of Forensic Sciences*, vol. 43, no. 3, pp. 509-513, 1998.

[31]   M. Gaft and L. Nagli, "UV gated raman spectroscopy for standoff detection of explosives," *Optical Materials-Amsterdam*, vol. 30, no. 11, pp. 1739-1746, 2008.

[32]   G. Comanescu, C. Manka, J. Grun, S. Nikitin, and D. Zabetakis, "Identification of explosives with two-dimensional ultraviolet resonance raman spectroscopy." *Applied Spectroscopy*, vol. 62, no. 8, pp. 833-839, Aug. 2008.

[33]   S. M. Angel, T. J. Kulp, and T. M. Vess, "Remote-raman spectroscopy at intermediate ranges using low-power cw lasers." *Applied Spectroscopy*, vol. 46, no. 7, pp. 1085-1091, Jul. 1992.

[34]   M. D. Ray, A. J. Sedlacek, and M. Wu, "Ultraviolet mini-Raman lidar for stand-off, in situ identification of chemical surface contaminants," *Review of Scientific Instruments*, vol. 71, pp. 3485-3489, 2000.

[35]   S. K. Sharma, A. K., Misra, and B. Sharma, "Portable remote raman system for monitoring hydrocarbon, gas hydrates and explosives in the environment," *Spectrochimica Acta Part A*, vol. 61, no. 10, pp. 2404-2412, 2005.

[36]   L. Nagli, M. Gaft, Y. Fleger, and M. Rosenbluh, "Absolute raman cross-sections

of some explosives: trend to UV," *Optical Materials-Amsterdam*, vol. 30, no. 11, pp. 1747-1754, 2008.

[37]   J. M. Dudik, C. R. Johnson, and S. A. Asher, "Wavelength dependence of the preresonance raman cross sections of CH_3CN, SO_4^{2-}, ClO_4^-, and NO_3^-," *Journal of Chemical Physics*, vol. 82, no. 4, pp. 1732-1740, Feb. 1985.

[38]   Y. J. Tian, J. Zuo, L.-Y. Zhang, Z.-W. Li, S.-Q. Gao, and G.-H. Lu, "Study of resonance Raman cross section of aqueous β-carotene at low concentrations," *Applied Physics B Lasers and Optics*, vol. 87, no. 4, pp. 727-730, 2007.

[39]   R. P. Feynman, R. B. Leighton, R. B and M. L. Sands, *The Feynman Lectures on Physics*. Reading, Mass: Addison-Wesley Pub, 1963.

[40]   S. D. Christesen, J. J. Pendell Jones, J. M. Lochner and A. M. Hyre, "Ultraviolet raman spectra and cross-sections of the G-series nerve agents." *Applied Spectroscopy,* vol. 62, no. 10, pp. 1078-83, Oct. 2008.

[41]   P. A. Jansson, *Deconvolution: With Applications in Spectroscopy*. New York: Academic Press, 1984.

[42]   O. Sandus and N. Slagg, *Reactions of Aromatic Nitrocompounds. I. Photochemistry*, Ft. Belvoir: Defense Technical Information Center, 1972.

[43]   C. Reichardt, *Solvents and solvent effects in organic chemistry*. Weinheim, Federal Republic of Germany: VCH, 1988.

[44]   P. W. Cooper, *Explosives Engineering*. Hoboken, N.J.: Wiley, 2008.

[45]   G. Eckhardt, and W. G. Wagner, "On the calculation of absolute raman scattering cross sections from raman scattering coefficients," *Journal of Molecular Spectroscopy*, vol. 19, pp. 407-411, 1966.

[46]   W. C. Mallard and J. W. Straley, "Vibrational intensities in halogenated methanes. III. The interpretation of solution data," *The Journal of Chemical Physics*, vol. 27, pp. 877-879, Oct. 1957.

[47]   L. Onsager, "Electric Moments of Molecules in Liquids," *Journal of the American Chemical Society*, vol. 58, no. 8, pp. 1486-1493, Aug 1936.

[48]   N. Abe, M. Wakayama, and M. Ito, "Absolute raman intensities of solids," *Journal of the Raman Spectroscopy*, vol. 6, no. 1, pp. 1486-1493, 1977.

[49]   S. R. Ahmad and V. G. Foster, "The local-field effect in raman scattering," *Journal of Physics D: Applied Physics*, vol. 31, pp. 2677-2685, 1997.

INITIAL DISTRIBUTION LIST

1.   Defense Technical Information Center
      Ft. Belvoir, Virginia

2.   Dudley Knox Library
      Naval Postgraduate School
      Monterey, California

3.   Dr. J. Chance Carter
      Lawrence Livermore National Laboratory
      Livermore, California

4.   Professor Craig Smith
      Naval Postgraduate School
      Monterey, California

5.   Professor Ronald Brown
      Naval Postgraduate School
      Monterey, California

6.   Lee Mastroianni
      Office of Naval Research, Code 30
      Arlington, Virginia

7.   Larry Mixson
      Naval Surface Warfare Center-Panama City
      Panama City, Florida

8.   Dr. John Wilkinson
      Naval Surface Warfare Center-Indian Head
      Indian Head, Maryland

9.   Dr. Jeff Terry
      Illinois Institute of Technology
      Chicago, Illinois

10.   Marine Corps Representative
      Naval Postgraduate School
      Monterey, California

11.   Director, Training and Education, MCCDC, Code C46
      Quantico, Virginia

12.	Director, Marine Corps Research Center, MCCDC, Code C40RC
	Quantico, Virginia

13.	Marine Corps Tactical Systems Support Activity (Attn: Operations Officer)
	Camp Pendleton, California